

# Isochrone fitting of Galactic globular clusters – III. NGC 288, NGC 362, and NGC 6218 (M12)

George A. Gontcharov,<sup>1\*</sup> Maxim Yu. Khovritchev,<sup>1,2</sup> Aleksandr V. Mosenkov,<sup>1,3</sup>

Vladimir B. Il'in,<sup>1,2,4</sup> Alexander A. Marchuk,<sup>1,2</sup> Sergey S. Savchenko,<sup>1,2,5</sup>

Anton A. Smirnov,<sup>1,2</sup> Pavel A. Usachev,<sup>1,2,5</sup> and Denis M. Poliakov<sup>1,2</sup>

<sup>1</sup>Central (Pulkovo) Astronomical Observatory, Russian Academy of Sciences, Pulkovskoye chaussee 65/1, St. Petersburg 196140, Russia

<sup>2</sup>Saint Petersburg State University, Universitetskij pr. 28, St. Petersburg 198504, Russia

<sup>3</sup>Department of Physics and Astronomy, N283 ESC, Brigham Young University, Provo, UT 84602, USA

<sup>4</sup>Saint Petersburg University of Aerospace Instrumentation, Bol. Morskaya ul. 67A, St. Petersburg 190000, Russia

<sup>5</sup>Special Astrophysical Observatory, Russian Academy of Sciences, 369167 Nizhnij Arkhyz, Russia

Accepted XXX. Received YYY; in original form ZZZ

## ABSTRACT

We present new isochrone fits to colour–magnitude diagrams of the Galactic globular clusters NGC 288, NGC 362, and NGC 6218 (M12). We utilize a lot of photometric bands from the ultraviolet to mid-infrared by use of data from the *HST*, *Gaia*, unWISE, Pan-STARRS, and other photometric sources. In our isochrone fitting we use theoretical models and isochrones from the Dartmouth Stellar Evolution Program and Bag of Stellar Tracks and Isochrones for  $\alpha$ –enhanced abundance  $[\alpha/\text{Fe}] = +0.40$ , different helium abundances, and a metallicity of about  $[\text{Fe}/\text{H}] = -1.3$  adopted from the literature. We derive the most probable distances  $8.96 \pm 0.05$ ,  $8.98 \pm 0.06$ , and  $5.04 \pm 0.05$  kpc, ages  $13.5 \pm 1.1$ ,  $11.0 \pm 0.6$ , and  $13.8 \pm 1.1$  Gyr, extinctions  $A_V = 0.08 \pm 0.03$ ,  $0.11 \pm 0.04$ , and  $0.63 \pm 0.03$  mag, and reddenings  $E(B - V) = 0.014 \pm 0.010$ ,  $0.028 \pm 0.011$ , and  $0.189 \pm 0.010$  mag for NGC 288, NGC 362, and NGC 6218, respectively. The distance estimates from the different models are consistent, while those of age, extinction, and reddening are not. The uncertainties of age, extinction, and reddening are dominated by some intrinsic systematic differences between the models. However, the models agree in their relative age estimates: NGC 362 is  $2.6 \pm 0.5$  Gyr younger than NGC 288 and  $2.8 \pm 0.5$  Gyr younger than NGC 6218, confirming age as the second parameter for these clusters. We provide reliable lists of the cluster members and precise cluster proper motions from the *Gaia* Early Data Release 3.

**Key words:** Hertzsprung–Russell and colour–magnitude diagrams – dust, extinction – globular clusters: general – globular clusters: individual: NGC 288, NGC 362, NGC 6218 (M12)

## 1 INTRODUCTION

In Gontcharov, Mosenkov & Khovritchev (2019, hereafter Paper I) and Gontcharov, Khovritchev & Mosenkov (2020, hereafter Paper II) we presented isochrone fits to colour–magnitude diagrams (CMDs) of the Galactic globular clusters (GCs) NGC 5904 (M5) and NGC 6205 (M13). We utilized accurate photometry of individual stars in many ultraviolet (UV), optical, and infrared (IR) bands by use of datasets from the *Hubble Space Telescope* (*HST*), *Gaia* Data Release 2 (DR2, Gaia Collaboration et al. 2018), *Wide-field Infrared Survey Explorer* (*WISE*, Wright et al. 2010), Panoramic Survey Telescope and Rapid Response System Data Release I (Pan-STARRS, PS1, Bernard et al. 2014; Chambers et al. 2016), and other photometric sources. In our isochrone fitting we used the Dartmouth Stellar Evolution Program (DSEP, Dotter et al. 2007)<sup>1</sup>, a Bag of Stellar Tracks and Isochrones (BaSTI-IAC, Hidalgo et al. 2018)<sup>2</sup>, and other

theoretical stellar evolution models and related isochrones. We employed the models for both the solar-scaled and  $\alpha$ –helium–enhanced abundances, with spectroscopic metallicities adopted from the literature.

All or almost all GCs contain multiple stellar populations (Monelli et al. 2013). In spite of this, a dominant population or a mix of populations can be accurately fitted in some CMDs of some GCs. NGC 5904 and NGC 6205 are examples of such GCs. In each CMD, except for some in the UV, we derived age, distance, and reddening for a dominant population or a mix of populations by isochrone fitting for different stages of stellar evolution, which can be well recognized in the CMDs. They are the main sequence (MS), its turn-off (TO), the subgiant branch (SGB), red giant branch (RGB), horizontal branch (HB), and asymptotic giant branch (AGB). Moreover, the models underlying these isochrones were verified by this fitting.

The derived distances and ages are different for the UV, optical, and IR photometry used, while the derived ages and reddenings are different for the different models. However, we obtained convergent estimates of the most probable distances and extinctions in all the

\* E-mail: georgegontcharov@yahoo.com

<sup>1</sup> <http://stellar.dartmouth.edu/models/>

<sup>2</sup> <http://basti-iac.oa-abruzzo.inaf.it/index.html>

bands, but less consistent estimates of ages. The extinctions appear to be twice as high as generally accepted for these GCs. We determined empirical extinction laws (dependence of extinction on wavelength), which agree with the law of [Cardelli, Clayton & Mathis \(1989\)](#), hereafter CCM89) with the best-fitting extinction-to-reddening ratio  $R_V \equiv A_V/E(B-V) = 3.6 \pm 0.05$  and  $3.1^{+1.6}_{-1.1}$  for NGC 5904 and NGC 6205, respectively.

The aim of this paper is to expand our research of Galactic GCs by exploiting a multiband photometry and up-to-date theoretical stellar evolution models for the other three GCs NGC 288, NGC 362, and NGC 6218 (M12), despite the presence of multiple populations in these clusters ([Monelli et al. 2013](#); [Milone et al. 2017](#)). Following [Paper I](#) and [Paper II](#), we adopt the spectroscopic metallicity and  $\alpha$ -helium-enhancement from the literature in order to obtain the most probable ages, distances, and empirical extinction laws for these GCs. Also, we estimate the accuracy and consistency of the models/isochrones under consideration.

As this is the third paper in this series devoted to investigation of GCs, the full details of our analysis, which we carry out in this study, are given in our [Paper I](#) and [Paper II](#). We refer the interested reader to those papers, especially to appendix A of [Paper II](#), although throughout this paper we briefly describe some crucial points of those studies.

This paper is organized as follows. We describe some key properties of NGC 288, NGC 362, and NGC 6218 in Sect. 2. In Sect. 3 we describe the photometry used, our cleaning of the datasets and creation of the fiducial sequences in the CMDs. In Sect. 4 we describe the theoretical models and corresponding isochrones used. The results of our isochrone fitting with their discussion are presented in Sect. 5. We summarize our main findings and conclusions in Sect. 6.

## 2 PROPERTIES OF THE CLUSTERS

We select these GCs for our study due to a rich photometric material available for the astronomical community, a rather low foreground and differential reddening<sup>4</sup>, as well as accurate spectroscopic estimates of their metallicity. Some general properties of NGC 288, NGC 362, and NGC 6218 (M12) are presented in Table 1.

These GCs are of particular interest since NGC 288 is close to the South Galactic Pole, while NGC 362 is located in the sky about 2° south (in Galactic coordinates) of the optical centre of the Small Magellanic Cloud (SMC). The latter means that SMC stars represent background for NGC 362 and inevitably contaminate any CMD for this cluster. This contamination should be removed, for example, by use of the proper motions (PMs) from the *Gaia* Early Data Release 3 (EDR3, [Gaia Collaboration et al. 2021a](#)), as done in Sect. 3.2.

Moreover, NGC 288 and NGC 362 are a well studied second-parameter pair. This means that, being of a similar metallicity,  $\alpha$ -enrichment, and even distance, these GCs have different HB morphologies: NGC 288 and NGC 362 have their HBs almost completely consisting of stars on the blue and red side of the instability strip, respectively. The HB of NGC 6218 is rather similar to that of NGC 288. Moreover, NGC 5904, studied by us in [Paper I](#), has a similar metallicity. Hence, all four GCs should be considered as a

second-parameter quartet ([VandenBerg et al. 2013](#)). A lot of studies (e.g. [Bolte 1989](#); [Lee, Demarque & Zinn 1994](#); [Bellazzini et al. 2001](#); [Marín-Franch et al. 2009](#)) have discussed whether age is the second parameter after metallicity which is responsible for this HB difference. In particular, [Bolte \(1989\)](#) found an age difference as large as 5 Gyr between NGC 288 and NGC 362, in contrast to [Marín-Franch et al. \(2009\)](#) who found a nearly zero age difference<sup>5</sup>. Based on the most precise data and models, we intend to answer whether age is the second parameter for these GCs.

We adopt models with [Fe/H] close to that from [Carretta et al. \(2009\)](#), as indicated in Sect. 4. In contrast to [Paper I](#) and [Paper II](#), we check [Fe/H] from the isochrone fitting for the tilt of the RGB. Brighter parts of the RGB are affected by saturation and crowding. This leads to a systematic uncertainty of about 0.1 dex in the [Fe/H] derived from the RGB tilt. However, we conclude that the observed RGB tilt certainly implies  $-1.4 < [\text{Fe}/\text{H}] < -1.2$  for all the CMDs.

All these GCs have two dominating populations ([Milone et al. 2017](#); [Lardo et al. 2018](#)). Both populations are  $\alpha$ -enriched with  $0.1 < [\alpha/\text{Fe}] < 0.4$  ([Carretta et al. 2010](#); [Marsakov, Koval' & Gozha 2019](#); [Horta et al. 2020](#)), but differ in helium abundance<sup>6</sup>. It would be reasonable to assume helium content  $Y \approx 0.248$  and  $Y \approx 0.275$  for the primordial and helium-enriched populations, respectively ([Piotto et al. 2013](#); [Wagner-Kaiser et al. 2016](#); [Milone et al. 2018](#)).

In Table 1 we provide both extinction  $A_V$  and reddening  $E(B-V)$ , since some of their estimates are based on a non-CCM89 extinction law. The extinction and reddening estimates from the 2D dust emission maps of [Schlegel, Finkbeiner & Davis \(1998\)](#), [Schlafly & Finkbeiner \(2011\)](#), and [Meisner & Finkbeiner \(2015\)](#) are averaged over the fields of the GCs and rounded to 0.01 mag. This value nearly corresponds to the uncertainty of the mean reddening in the fields of these GCs due to differential reddening. Some inconsistency of the extinction and reddening estimates in Table 1 is evident. This will be discussed in Sect. 5.1.

Table 1 gives the differential reddening from [Bonatto, Campos & Kepler \(2013, hereafter BCK13\)](#). Generally speaking, differential reddening should be lower than a mean reddening of a cluster. Therefore, a rather high mean differential reddening from BCK13  $\delta E(B-V) = 0.047 \pm 0.018$  mag for NGC 288, in particular, its maximum value  $\delta E(B-V)_{\text{max}} = 0.091$  mag hardly reconciles with rather low reddening estimates  $0.01 < E(B-V) < 0.03$  mag in Table 1. To a lesser extent, this applies to NGC 362. However, the differential reddening measured by BCK13 is very hard to distinguish from the systematic variations of colours in a cluster field due to other reasons (hereafter field effects). Such effects include systematic photometric errors, distortion, telescope breathing, telescope focus change, stellar population variations, and others ([Anderson et al. 2008](#)). Generally speaking, these effects influence different photometric filters in different ways, so their observed manifestation is a slight colour shift of a cluster fiducial sequence as a function of location in the cluster field. ‘On average this shift is zero, but the trend with position can be as large as  $\pm 0.02$  mag’ ([Anderson et al. 2008](#)). Indeed, we found such a level of the colour variations in the field of NGC 6205 in [Paper II](#). We examine differential reddening and related field effects, which appear as fiducial sequence colour variations over the cluster field, in Sect. 3. We add some notes on these effects in Sect. 5.1.

<sup>3</sup> The commonly used database of GCs by [Harris \(1996\)](#) (<https://www.physics.mcmaster.ca/~harris/mwgc.dat>), 2010 revision.

<sup>4</sup> In this paper by differential reddening, we mean variations of reddening over a cluster field, but see our note at the end of this section.

<sup>5</sup> ‘Our results indicate that NGC 0288 and NGC 0362 have the same age within  $\pm 0.9$  Gyr’ ([Marín-Franch et al. 2009](#)).

<sup>6</sup> ‘There is a broad consensus on the similarity in chemical composition between NGC 288 and NGC 362’ ([Bellazzini et al. 2001](#)).

**Table 1.** Some properties of the clusters under consideration. A typical precision of the data is a few units of the last decimal place, unless otherwise stated. The *Gaia* EDR3 median parallax is calculated by us in Sect. 3.2.

Property	NGC 288	NGC 362	NGC 6218
R.A. J2000 (h m s) from Goldsbury et al. (2010)	00 52 45	01 03 14	16 47 14
Decl. J2000 (° ' ") from Goldsbury et al. (2010)	−26 34 57	−70 50 56	−01 56 55
Galactic longitude (°) from Goldsbury et al. (2010)	151.2851	301.5330	15.7151
Galactic latitude (°) from Goldsbury et al. (2010)	−89.3804	−46.2474	+26.3134
Angular diameter (arcmin) from Bica et al. (2019)	15	15	19
Distance from the Sun (kpc) from Harris (1996), 2010 revision <sup>3</sup>	8.9	8.6	4.8
Distance from the Sun (kpc) from Baumgardt & Vasiliev (2021)	8.99 ± 0.09	8.83 ± 0.10	5.11 ± 0.05
<i>Gaia</i> EDR3 median parallax (mas)	0.114 ± 0.011	0.119 ± 0.011	0.210 ± 0.011
[Fe/H] from Carretta et al. (2009)	−1.32 ± 0.02	−1.30 ± 0.04	−1.33 ± 0.02
[Fe/H] from Marsakov, Koval' & Gozha (2019)	−1.37 ± 0.04	−1.20 ± 0.08	−1.35 ± 0.05
[ $\alpha$ /Fe] from Carretta et al. (2010)	0.42	0.30	0.41
Mean differential reddening $\delta E(B - V)$ (mag) from BCK13	0.047 ± 0.018	0.032 ± 0.009	0.027 ± 0.008
Maximum differential reddening $\delta E(B - V)_{\max}$ (mag) from BCK13	0.091	0.056	0.056
$A_V$ (mag) from Harris (1996), 2010 revision	0.09	0.16	0.59
$A_V$ (mag) from Schlegel, Finkbeiner & Davis (1998)	0.04	0.10	0.54
$A_V$ (mag) from Schlafly & Finkbeiner (2011)	0.03	0.09	0.47
$A_V$ (mag) from Meisner & Finkbeiner (2015)	0.05	0.12	0.50
$E(B - V)$ (mag) from Harris (1996), 2010 revision	0.03	0.05	0.19
$E(B - V)$ (mag) from Schlegel, Finkbeiner & Davis (1998)	0.01	0.03	0.18
$E(B - V)$ (mag) from Schlafly & Finkbeiner (2011)	0.01	0.03	0.15
$E(B - V)$ (mag) from Meisner & Finkbeiner (2015)	0.01	0.04	0.16

### 3 PHOTOMETRY

As discussed in Paper I and Paper II, in order to derive the accurate distance, age, and reddening for a GC, we prefer using photometric datasets covering, at least, the cluster HB, SGB, TO, and part of the RGB between the HB and SGB.

We select *Gaia* EDR3, Pan-STARRS, and some other initial samples/datasets of the cluster members, within the cluster diameters from Table 1, by use of the Vizier and X-Match services of the Centre de Données astronomiques de Strasbourg (Ochsenbein, Bauer & Marcout 2000)<sup>7</sup>. Then the initial datasets are cleaned, as described in Sect. 3.1.

The adopted cluster diameters and related truncation radii are slightly smaller than those derived by de Boer et al. (2019) and in some other recent studies. However, for isochrone fitting, we do not need a complete sample of stars, but we do need a cleanest sample with a minimised contamination. Adopting such truncation radii, we may lose few peripheral cluster members, but, on the other hand, we ensure a high percentage of members among the selected stars.

Selection of cluster members from *Gaia* EDR3 can be more sophisticated and precise by use of its very accurate PMs. Therefore, unlike the other datasets in our study, we select initial *Gaia* EDR3 samples within initial radii which are six times larger than those used for the other datasets. We use the periphery of these fields for estimating the star count surface density of the Galactic field background. Its subtraction allows us to derive some empirical truncation radii while cleaning the initial *Gaia* EDR3 samples, as described in Sect. 3.2.

We use the following datasets (see Table 2):

(i) the *HST* Wide Field Camera 3 (WFC3) UV Legacy Survey of Galactic Globular Clusters (the *F*275W, *F*336W and *F*438W filters) and the Wide Field Channel of the Advanced Camera for Surveys (ACS; the *F*606W and *F*814W filters) survey of Galactic globular clusters (Nardiello et al. 2018)<sup>8</sup>,

(ii) Strömberg *uvby* photometry from the 1.54 m Danish Telescope, European Southern Observatory (ESO), La Silla (Grundahl et al. 1999, hereafter GCL99),

(iii) a compilation of the *UBVR* photometry (SPZ19)<sup>9</sup>,

(iv) *UBVI* photometry from the Magellanic Clouds Photometric Survey (MCPS) with the 1 m Las Campanas Swope telescope (Zaritsky et al. 2002),

(v) photometry from Piotto et al. (2002) in the *F*439W and *F*555W filters from the *HST* Wide Field and Planetary Camera 2 (WFPC2) transformed by the authors into the *B* and *V* magnitudes<sup>10</sup>,

(vi) *BV* photometry with the Wide Field Imager (WFI) mounted on the 2.2 m telescope, ESO, La Silla (Sollima et al. 2016, hereafter SFL16),

(vii) the fiducial sequence in the '*B - V* versus *V*' plane derived by Bolte (1992) from the photometry with the 4 m and 0.9 m telescopes of the Cerro-Tololo Inter-American Observatory (CTIO),

(viii) *BVI* photometry with the Kitt Peak National Observatory (KPNO) 0.9 m telescope (Hargis, Sandquist & Bolte 2004, hereafter HSB04),

(ix) *BV* photometry with the 2.5 m du Pont telescope, Las

<sup>8</sup> <http://groups.dfa.unipd.it/ESPG/treasury.php>

<sup>9</sup> <http://cdsarc.u-strasbg.fr/viz-bin/cat/J/MNRAS/485/3042>

<sup>10</sup> We use the *B* and *V* instead of *F*439W and *F*555W filters since they are better defined by the models used.

<sup>7</sup> <http://cds.u-strasbg.fr>

Campanas (Zloczewski et al. 2012; Kaluzny et al. 2015, hereafter ZKR12),

(x) The Dark Energy Survey (DES) Data Release 1 photometry in the  $g_{\text{DECam}}$ ,  $r_{\text{DECam}}$ ,  $i_{\text{DECam}}$ , and  $z_{\text{DECam}}$  filters obtained by Abbott et al. (2018) with the Dark Energy Camera (DECam) mounted on the 4 m Blanco telescope at CTIO,

(xi) Parallel-Field Catalogues (the  $F475W$  and  $F814W$  filters) of the *HST* UV Legacy Survey of Galactic Globular Clusters with ACS (Simioni et al. 2018),

(xii) Pan-STARRS photometry in the  $g_{\text{PS1}}$ ,  $r_{\text{PS1}}$ ,  $i_{\text{PS1}}$ ,  $z_{\text{PS1}}$ , and  $y_{\text{PS1}}$  filters (Chambers et al. 2016) and related fiducial sequences derived by Bernard et al. (2014),

(xiii) *Gaia* DR2 and EDR3 photometry in the  $G$ ,  $G_{\text{BP}}$  and  $G_{\text{RP}}$  filters (Gaia Collaboration et al. 2018, 2021b),

(xiv)  $VI$  photometry with the 2.2 m ESO/MPI telescope, La Silla, equipped with the EFOSC2 camera, as well as the fiducial sequence (Bellazzini et al. 2001, hereafter BPF01),

(xv)  $VI$  photometry with 0.91 m DUTCH telescope, ESO, La Silla (Rosenberg et al. 2000, hereafter RPS00),

(xvi) SkyMapper Southern Sky Survey DR3 (SMSS, SMSS DR3) photometry in the  $g_{\text{SMSS}}$ ,  $r_{\text{SMSS}}$ ,  $i_{\text{SMSS}}$ , and  $z_{\text{SMSS}}$  filters (Onken et al. 2019)<sup>11</sup>,

(xvii) the fiducial sequence in the ‘ $J - K$  versus  $K$ ’ plane derived by Davidge & Harris (1997) from the photometry with the 3.6 m Canada–France–Hawaii Telescope (CFHT),

(xviii)  $J$  and  $K_s$  photometry obtained by Cohen et al. (2015) with Infrared Side Port Imager (ISPI) mounted on the 4 m Blanco telescope at CTIO and calibrated by use of the Two Micron All-Sky Survey (2MASS, Skrutskie et al. 2006) stars,

(xix) *Wide-field Infrared Survey Explorer (WISE)* photometry in the  $W1$  filter from the unWISE catalogue (Schlafly et al. 2019),

(xx) photometry in the  $3.6\text{-}\mu\text{m}$  filter of the *Spitzer* Space Telescope Infrared Array Camera (IRAC) obtained by Gordon et al. (2011) within the Surveying the Agents of Galaxy Evolution in the Tidally-Disrupted, Low-Metallicity Small Magellanic Cloud (SAGE-SMC, SAGE)<sup>12</sup>.

Each star has a photometry in some but not all filters. Totally 33, 26 and 26 filters are exploited for NGC 288, NGC 362, and NGC 6218, respectively. They span a wide wavelength range between the UV and middle IR. For each filter, Table 2 presents the effective wavelength  $\lambda_{\text{eff}}$  in nm, number of stars and the median photometric precision after rejecting the poor photometry. The rejection procedure is described in Sect. 3.1 and 3.2. The original datasets typically contain many more stars. The median precision is calculated from the precisions stated by the authors of the datasets used. The median precision is used for calculating predicted uncertainties of the derived age, distance and reddening, as described in appendix A of Paper II and in Sect. 5.

To be fitted by a theoretical isochrone, data should be presented by a fiducial sequence, i.e. a colour–magnitude relation for single stars. Such a sequence is calculated as a locus of the number density maxima in some colour–magnitude bins. Some details and examples are given in section 3 of Paper II.

The stellar populations are segregated at the HB and AGB in almost all CMDs with the UV and optical filters, as well as at the RGB in the following CMDs<sup>13</sup>:  $F275W - F336W$ ,  $F336W - F438W$ ,  $U - B$ ,  $R - I$ ,

Strömgren  $u - v$  for all the GCs and  $F438W - F606W$  for NGC 288. In such a case, each population is presented by its own fiducial sequence, which, in turn, is fitted by its own primordial or helium-enriched isochrone (the DSEP helium-enriched isochrone with  $Y = 0.275$  is interpolated in each CMD from the isochrones with  $Y = 0.2475$  and  $0.33$ <sup>14</sup>). For the remaining cases, we consider and fit an unresolved mix of the populations. Since two populations, with  $Y \approx 0.248$  and  $Y \approx 0.275$ , are well presented in these GCs (Milone et al. 2017), it is reasonable to adopt the average value  $Y \approx 0.26$  for their mix. This mix is presented by a fiducial sequence, which, in turn, is fitted by an isochrone for  $Y = 0.26$  interpolated in each CMD between the primordial and helium-enriched isochrones of the same model, distance, reddening, and age<sup>15</sup> (see Sect. 4).

For our clusters, some important CMD domains have a small number of stars: e.g. red HBs of NGC 288 and NGC 6218. In such cases, a fiducial point is defined by a few or even only one star, if the photometry of such star/stars is rather precise, i.e. if a colour and a magnitude of such a fiducial point can be defined within  $\pm 0.04$  mag. Since we use a lot of fiducial points to derive distance, age, and reddening, such an uncertainty of a fiducial point is negligible w.r.t. total uncertainty (see the balance of uncertainties in appendix A of Paper II).

As an example, the fiducial sequences for the *Gaia* EDR3 datasets are presented in Table 3. All other fiducial sequences can be provided on request.

Similar to Paper II, we analyse variations of the fiducial sequence colour over the cluster fields for all the CMDs, which are based on the largest datasets of *HST* ACS/WFC3, Pan-STARRS, GCL99 and SPZ19. We calculate partial fiducial sequences, i.e. the ones for different parts of the field, along the RGB, SGB, TO and a brighter part of the MS by use of a moving window with about 2000 stars. As for NGC 6205 in Paper II, we find significant variations of the fiducial sequence colour only for some datasets and only in most crowded central parts of GCs, up to 2 arcmin. In such cases, stars in the central parts are removed. Elsewhere, we find rather small fiducial sequence colour variations at a level of  $\Delta(B - V) < 0.02$  mag. Such a level agrees with the estimates of Anderson et al. (2008) as well as with a rather small mean differential reddening  $\delta E(B - V)$  in the fields of NGC 362 and NGC 6218, obtained by BCK13 and presented in Table 1. Given such a small effect for the largest datasets, we suggest a similar effect for the others. As shown in Paper II, since we consider the entire cluster fields, this effect is averaged. Therefore, this makes a negligible contribution to the total uncertainties and, hence, we do not take it into account further.

### 3.1 Cleaning the datasets

Cleaning the original datasets from poor photometry for our GCs is similar to what was done for NGC 6205 in Paper II.

We select stars with a photometric error of less than 0.1 mag. A higher limit of  $< 0.15$  mag is applied to MCPS and SAGE due to their less precise photometry (see Table 2).

For the datasets of SPZ19, GCL99, SFL16, Piotto et al. (2002),

<sup>14</sup> Since the initial isochrones are close to each other in any CMD and since they are presented by the same evolutionary points, such interpolation in colour–magnitude planes is robust, with uncertainties less than 0.01 mag.

<sup>15</sup> The helium-enriched population may be a few hundred Myr younger, but this age difference is negligible w.r.t. precision of the derived ages, indicated in Sect. 5.

<sup>11</sup> <https://skymapper.anu.edu.au>

<sup>12</sup> <http://sage.stsci.edu/>

<sup>13</sup> We find no CMD for these GCs with the populations segregated at the SGB, TO, or MS.



**Table 2.** The effective wavelength  $\lambda_{\text{eff}}$  (nm), number of stars and median precision of the photometry (mag) for the datasets and filters under consideration.

Telescope, dataset, reference	Filter	$\lambda_{\text{eff}}$	Number of stars / Median precision		
			NGC 288	NGC 362	NGC 6218
<i>HST</i> /WFC3 (Nardiello et al. 2018)	<i>F</i> 275W	285	3454 / 0.02	11757 / 0.02	5936 / 0.02
<i>HST</i> /WFC3 (Nardiello et al. 2018)	<i>F</i> 336W	340	5226 / 0.01	17105 / 0.02	8632 / 0.01
1.54 m Danish Telescope, ESO, La Silla (GCL99)	Strömgren <i>u</i>	349	9566 / 0.03	5263 / 0.03	
Various (SPZ19)	<i>U</i>	366	10144 / 0.02		12045 / 0.01
1 m Las Campanas Swope telescope, MCPS (Zaritsky et al. 2002)	<i>U</i>	366		2640 / 0.10	
1.54 m Danish Telescope, ESO, La Silla (GCL99)	Strömgren <i>v</i>	414	10936 / 0.02	6876 / 0.02	
<i>HST</i> /WFC3 (Nardiello et al. 2018)	<i>F</i> 438W	438	4309 / 0.02	15348 / 0.02	10588 / 0.01
<i>HST</i> /WFPC2 (Piotto et al. 2002)	<i>B</i> (from <i>F</i> 439W)	452		14325 / 0.04	4186 / 0.04
Various (SPZ19)	<i>B</i>	452	13910 / 0.01		12129 / 0.01
1 m Las Campanas Swope telescope, MCPS (Zaritsky et al. 2002)	<i>B</i>	452		6399 / 0.06	
2.2 m telescope, ESO, La Silla (SFL16)	<i>B</i>	452	9908 / 0.01		
4 m and 0.9 m telescopes, CTIO (Bolte 1992)	<i>B</i>	452	fiducial / 0.03		
0.9 m telescope, KPNO (HSB04)	<i>B</i>	452			11292 / 0.04
2.5 m du Pont telescope, Las Campanas (ZKR12)	<i>B</i>	452			7758 / 0.02
1.54 m Danish Telescope, ESO, La Silla (GCL99)	Strömgren <i>b</i>	469	12372 / 0.02	7135 / 0.02	
4 m Blanco telescope, CTIO, DECam, DES (Abbott et al. 2018)	<i>g</i> DECam	481	2940 / 0.01		
<i>HST</i> /ACS (Simioni et al. 2018)	<i>F</i> 475W	484			2776 / 0.01
Pan-STARRS (Bernard et al. 2014; Chambers et al. 2016)	<i>g</i> PS1	496	6902 / 0.02		10522 / 0.02
SkyMapper Sky Survey DR3 (Onken et al. 2019)	<i>g</i> SMSS	514	2217 / 0.02	2194 / 0.02	2498 / 0.02
<i>Gaia</i> DR2 (Gaia Collaboration et al. 2018)	<i>G</i> BP	539	1713 / 0.03	1054 / 0.03	2847 / 0.02
<i>Gaia</i> EDR3 (Gaia Collaboration et al. 2021b)	<i>G</i> BP	540	3923 / 0.03	4139 / 0.03	6231 / 0.03
1.54 m Danish Telescope, ESO, La Silla (GCL99)	Strömgren <i>y</i>	550	12373 / 0.02	7023 / 0.03	
<i>HST</i> /WFPC2 (Piotto et al. 2002)	<i>V</i> (from <i>F</i> 555W)	552		14325 / 0.06	4186 / 0.03
Various (SPZ19)	<i>V</i>	552	13928 / 0.01		12129 / 0.01
2.2 m telescope, ESO, La Silla (SFL16)	<i>V</i>	552	9908 / 0.01		
4 m and 0.9 m telescopes, CTIO (Bolte 1992)	<i>V</i>	552	fiducial / 0.02		
2.2 m ESO/MPI telescope, La Silla, EFOSC2 (BPF01)	<i>V</i>	552	10777 / 0.02	7271 / 0.03	
1 m Las Campanas Swope telescope, MCPS (Zaritsky et al. 2002)	<i>V</i>	552		6399 / 0.06	
0.91 m DUTCH telescope, ESO, La Silla (RPS00)	<i>V</i>	552		1391 / 0.02	
0.9 m telescope, KPNO (HSB04)	<i>V</i>	552			14019 / 0.03
2.5 m du Pont telescope, Las Campanas (ZKR12)	<i>V</i>	552			7758 / 0.01
<i>HST</i> /ACS (Nardiello et al. 2018)	<i>F</i> 606W	599	13170 / 0.01	38951 / 0.01	20344 / 0.01
SkyMapper Sky Survey DR3 (Onken et al. 2019)	<i>r</i> SMSS	615	2495 / 0.02	1917 / 0.02	3146 / 0.02
Pan-STARRS (Bernard et al. 2014; Chambers et al. 2016)	<i>r</i> PS1	621	7877 / 0.02		12195 / 0.01
<i>Gaia</i> DR2 (Gaia Collaboration et al. 2018)	<i>G</i>	642	1713 / 0.01	1054 / 0.01	2847 / 0.01
<i>Gaia</i> EDR3 (Gaia Collaboration et al. 2021b)	<i>G</i>	642	3923 / 0.01	4139 / 0.01	6231 / 0.01
4 m Blanco telescope, CTIO, DECam, DES (Abbott et al. 2018)	<i>r</i> DECam	644	3890 / 0.01		
Various (SPZ19)	<i>R</i>	659	13726 / 0.01		12111 / 0.01
Pan-STARRS (Bernard et al. 2014; Chambers et al. 2016)	<i>i</i> PS1	752	7885 / 0.02		13030 / 0.02
<i>Gaia</i> DR2 (Gaia Collaboration et al. 2018)	<i>G</i> RP	767	1713 / 0.02	1054 / 0.02	2847 / 0.01
<i>Gaia</i> EDR3 (Gaia Collaboration et al. 2021b)	<i>G</i> RP	774	3923 / 0.03	4139 / 0.03	6231 / 0.02
SkyMapper Sky Survey DR3 (Onken et al. 2019)	<i>i</i> SMSS	776	2981 / 0.02	2570 / 0.03	4098 / 0.02
4 m Blanco telescope, CTIO, DECam, DES (Abbott et al. 2018)	<i>i</i> DECam	784	4037 / 0.01		
<i>HST</i> /ACS (Nardiello et al. 2018)	<i>F</i> 814W	807	13170 / 0.01	38951 / 0.01	20344 / 0.01
<i>HST</i> /ACS (Simioni et al. 2018)	<i>F</i> 814W	807			2776 / 0.01
Various (SPZ19)	<i>I</i>	807	13898 / 0.01		12113 / 0.01
2.2 m ESO/MPI telescope, La Silla, EFOSC2 (BPF01)	<i>I</i>	807	10777 / 0.03	7271 / 0.04	
1 m Las Campanas Swope telescope, MCPS (Zaritsky et al. 2002)	<i>I</i>	807		5721 / 0.07	
0.91 m DUTCH telescope, ESO, La Silla (RPS00)	<i>I</i>	807		1391 / 0.03	
0.9 m telescope, KPNO (HSB04)	<i>I</i>	807			13913 / 0.04
Pan-STARRS (Bernard et al. 2014; Chambers et al. 2016)	<i>z</i> PS1	867	6094 / 0.02		12578 / 0.02
SkyMapper Sky Survey DR3 (Onken et al. 2019)	<i>z</i> SMSS	913	2375 / 0.03	1712 / 0.03	3435 / 0.02
4 m Blanco telescope, CTIO, DECam, DES (Abbott et al. 2018)	<i>z</i> DECam	927	3373 / 0.02		
Pan-STARRS (Bernard et al. 2014; Chambers et al. 2016)	<i>y</i> PS1	971	3706 / 0.03		6996 / 0.02
3.6 m CFHT telescope (Davidge & Harris 1997)	<i>J</i>	1234	fiducial / 0.05		
4 m Blanco telescope, CTIO, ISPI (Cohen et al. 2015)	2MASS <i>J</i>	1235		7412 / 0.02	
4 m Blanco telescope, CTIO, ISPI (Cohen et al. 2015)	2MASS <i>K<sub>s</sub></i>	2176		7412 / 0.03	
3.6 m CFHT telescope (Davidge & Harris 1997)	<i>K</i>	2193	fiducial / 0.05		
<i>WISE</i> , unWISE (Schlafly et al. 2019)	<i>W</i> 1	3317	794 / 0.03	764 / 0.01	1563 / 0.01
<i>Spitzer</i> , IRAC, SAGE (Gordon et al. 2011)	3.6 $\mu\text{m}$	3524		1559 / 0.09	

**Table 3.** The fiducial sequences for NGC 288, NGC 362, and NGC 6218  $G_{\text{BP}} - G_{\text{RP}}$  versus  $G_{\text{BP}} - G_{\text{RP}}$  based on the data of *Gaia* EDR3. The complete table is available online.

NGC 288		NGC 362		NGC 6218	
$RP$	$BP - RP$	$RP$	$BP - RP$	$RP$	$BP - RP$
17.60	-0.24	15.05	0.58	16.60	0.08
17.20	-0.20	14.90	0.72	16.05	0.12
16.90	-0.16	14.88	0.76	15.70	0.16
16.60	-0.12	14.86	0.80	15.40	0.20
16.20	-0.06	14.82	0.84	15.20	0.24
...	...	...	...	...	...

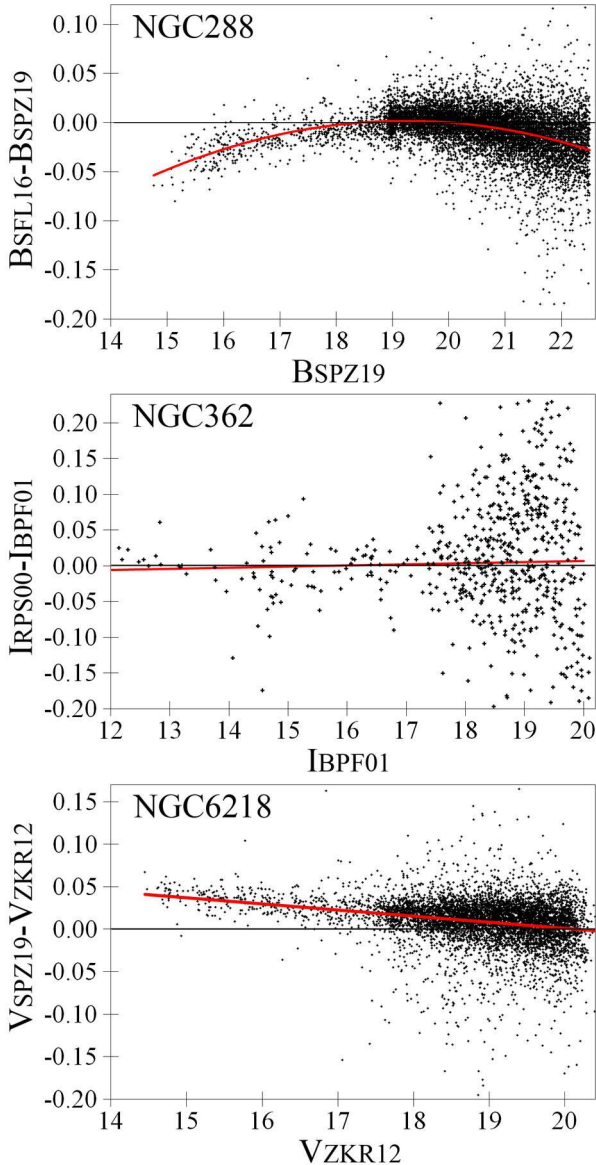


**Figure 1.** Some examples of dataset magnitude differences as functions of magnitude. The approximating functions from Table 4 are shown by the red curves.

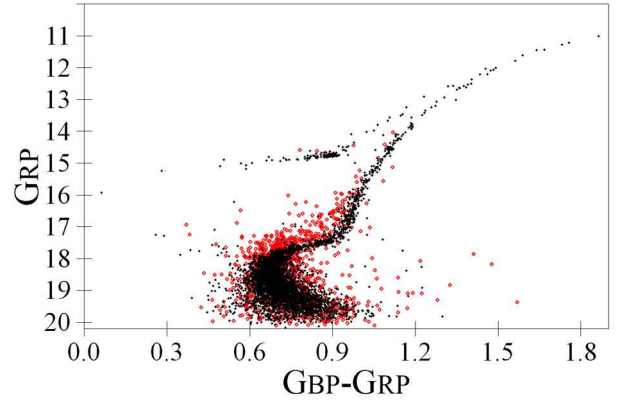


**Figure 2.**  $G_{\text{BP}} - G_{\text{RP}}$  versus  $G_{\text{RP}}$  CMD for NGC 362 stars with acceptable or unacceptable BP/RP excess factor, which are shown by black and red symbols, respectively, after applying the remaining cleaning of the sample.

**RPS00** and some others, we select stars with DAOPHOT *sharp* parameters  $|\text{sharp}| < 0.3$  and  $\chi < 3$ . For the HST WFC3 and ACS photometry we select stars with  $|\text{sharp}| < 0.15$ , membership probability  $> 0.9$  or  $-1$ , and quality fit  $> 0.9$ . For DES we select stars with extended source flags  $> 0.6$  in all the DES filters. For Pan-STARRS we select stars with the parameter ‘Maximum point-spread function weighted fraction of pixels totally unmasked from filter detections’  $> 0.9$  for all the filters under consideration. For the *Gaia* DR2 dataset, we select stars with a precise photometry as those with available data in all three *Gaia* bands and with an acceptable parameter  $\text{phot\_bp\_rp\_excess\_factor} > 1.3 + 0.06\text{bp\_rp}^2$ , as suggested by *Gaia* Collaboration et al. (2018).

For each cluster we have several datasets with photometry in the *BVI* filters. We cross-identify these datasets for a direct comparison. Their magnitude differences are presented as some functions of magnitude in Table 4. Some examples of these functions are shown in Fig. 1 by the red curves. Such magnitude differences at a level of few hundredths of a magnitude are common (see a detailed analysis by Anderson et al. 2008). As we do not know which dataset has the correct photometric system, we have to put the datasets on an average system. To do this, we use the functions from Table 4 in order to correct the magnitudes from these datasets keeping the same average magnitudes of their common stars. All the corrections are within a few hundredths of a magnitude. Since the datasets of Bolte (1992) and Piotto et al. (2002) cannot be cross-identified with the others, no correction is applied to them. We do not use them for creating the average photometric system, but we use them as is in the isochrone fitting.

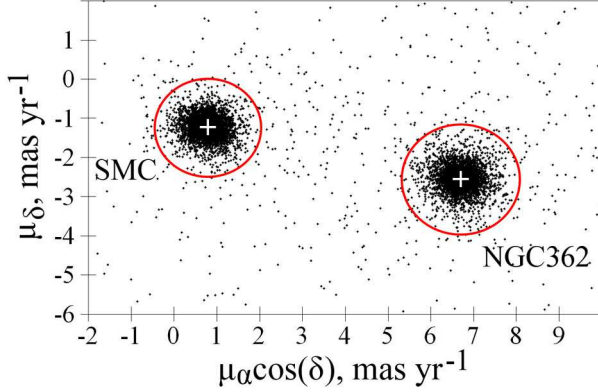
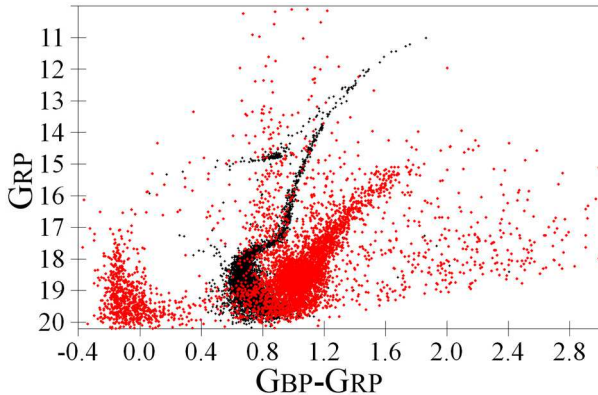
### 3.2 Cleaning the *Gaia* EDR3 datasets

Comparing *Gaia* DR2 with EDR3, we note that the latter, being a magnitude deeper, provides many more cluster stars, as is evident from Table 2. Also, *Gaia* EDR3 provides more precise parallaxes and PMs for these stars. This allows us to do a special cleaning of the *Gaia* EDR3 datasets.

We remove *Gaia* EDR3 stars with `duplicated_source=1` (Dup=1), `astrometric_excess_noise > 1` ( $\epsilon_i > 1$ ), or renormalised unit weight error exceeding 1.2 ( $\text{RUWE} > 1.2$ ). We remove foreground and background stars as those with measured parallax  $\varpi > 1/R + 3\sigma_\varpi$  or  $\varpi < 1/R - 3\sigma_\varpi$ , where  $R$  is the distance to the cluster derived by us (it is upgraded iteratively starting from the Harris 1996 values in Table 1), and  $\sigma_\varpi$  is the stated paral-

**Table 4.** Pairs of datasets with  $B$ ,  $V$ , and  $I$  filters: their differences as functions of magnitude.

Dataset pair	$\Delta B$	$\Delta V$	$\Delta I$
NGC 288			
SFL16-SPZ19	$-0.0028B^2 + 0.1067B - 1.0245$	$+0.0010V - 0.0194$	
BPF01-SPZ19		$-0.0050V + 0.0950$	$+0.0008I - 0.03$
BPF01-SFL16		$-0.0060V + 0.1144$	
NGC 362			
MCPS-RPS00		$+0.0024V - 0.0649$	$-0.0002I - 0.0035$
RPS00-BPF01		$+0.0011V - 0.0134$	$+0.0015I - 0.0236$
MCPS-BPF01		$+0.0035V - 0.0783$	$+0.0013I - 0.0271$
NGC 6218			
SPZ19-ZKR12	$-0.0047B + 0.0628$	$-0.0069V + 0.1396$	
HSB04-SPZ19	$-0.0010B + 0.0218$	$+0.0006V - 0.0178$	$+0.0009I - 0.0191$
HSB04-ZKR12	$-0.0057B + 0.0846$	$-0.0063V + 0.1218$	


**Figure 3.** The distribution of stars, selected within 18.7 arcmin of the NGC 362 centre, on the proper motion components ( $\text{mas yr}^{-1}$ ), after the remaining cleaning of the sample. The weighted mean PM and the selection area are shown by the white cross and red circle for the SMC (left) and NGC 362 (right).

**Figure 4.**  $G_{BP} - G_{RP}$  versus  $G_{RP}$  CMD for NGC 362 stars selected by their proper motion (black symbols) versus the SMC and other foreground and background stars (red symbols) after the remaining cleaning of the sample.

lax uncertainty. Also, we remove few stars without PMs. We select *Gaia* EDR3 stars with precise photometry as those with available data in all three *Gaia* bands and with an acceptable parameter `phot_bp_rp_excess_factor_corrected` (i.e.  $E(BP/RP)_{\text{Corr}}$ ) between  $-0.14$  and  $0.14$  (Gaia Collaboration et al. 2021b). Fig. 2 shows the *Gaia* EDR3 stars of NGC 362 with acceptable and unacceptable `phot_bp_rp_excess_factor_corrected` as black and red symbols, respectively, after applying the remaining cleaning of the sample. It is seen that the stars with unacceptable `phot_bp_rp_excess_factor_corrected` deviate systematically.

This cleaning removes almost all stars in a few central arcminutes of the cluster fields. The remaining stars in the centres do not show any systematics in the CMDs.

We select likely cluster members and derive systemic PMs of the clusters based on the positions and PM components  $\mu_\alpha \cos(\delta)$  and  $\mu_\delta$  of the stars. This procedure includes the following steps:

(i) The initial cluster centre coordinates are adopted from Goldsbury et al. (2010).

(ii) The initial cluster systemic PM components  $\overline{\mu_\alpha \cos(\delta)}$  and  $\overline{\mu_\delta}$  are adopted from Vasiliev & Baumgardt (2021, hereafter VB21).

(iii) The initial *Gaia* EDR3 sample is selected within 45, 45, and 57 arcmin from the centres of NGC 288, NGC 362, and NGC 6218, respectively.

(iv) We calculate the deviations of the individual PMs from the systemic PM as  $\sqrt{(\mu_\alpha \cos(\delta) - \overline{\mu_\alpha \cos(\delta)})^2 + (\mu_\delta - \overline{\mu_\delta})^2}$ .

(v) Initially, we remove stars with  $\sqrt{(\mu_\alpha \cos(\delta) - \overline{\mu_\alpha \cos(\delta)})^2 + (\mu_\delta - \overline{\mu_\delta})^2} > 2 \text{ mas yr}^{-1}$ , since the PM dispersion and stated *Gaia* EDR3 PM uncertainties specify a  $3\sigma$  limit, which rejects these stars as being unlikely cluster members.

(vi) We find the cluster truncation radius at a sharp drop of the cluster radial star number density profile, and select cluster members as stars within the truncation radius.

(vii) We calculate the standard deviations  $\sigma_{\mu_\alpha \cos(\delta)}$  and  $\sigma_{\mu_\delta}$  of the PM components of the members.

(viii) We cut the sample at  $3\sigma$ , i.e. only select stars with  $\sqrt{(\mu_\alpha \cos(\delta) - \overline{\mu_\alpha \cos(\delta)})^2 + (\mu_\delta - \overline{\mu_\delta})^2} < 3\sqrt{\sigma_{\mu_\alpha \cos(\delta)}^2 + \sigma_{\mu_\delta}^2}$  as cluster members.

(ix) We recalculate the mean coordinates of the cluster centre.

**Table 5.** The cluster systemic PMs (mas yr<sup>-1</sup>).

Cluster	Source	$\mu_{\alpha} \cos(\delta)$	$\mu_{\delta}$
NGC 288	This study	$4.147 \pm 0.005$	$-5.704 \pm 0.006$
	VB21	$4.164 \pm 0.024$	$-5.705 \pm 0.025$
	Vitral (2021)	$4.154 \pm 0.005$	$-5.700 \pm 0.005$
NGC 362	This study	$6.696 \pm 0.005$	$-2.543 \pm 0.005$
	VB21	$6.694 \pm 0.024$	$-2.536 \pm 0.024$
	Vitral (2021)	$6.680 \pm 0.011$	$-2.545 \pm 0.011$
NGC 6218	This study	$-0.204 \pm 0.005$	$-6.809 \pm 0.004$
	VB21	$-0.191 \pm 0.024$	$-6.801 \pm 0.024$
	Vitral (2021)	$-0.213 \pm 0.007$	$-6.811 \pm 0.007$

(x) We recalculate the systemic PM components as the weighted means of the individual PM components of the cluster members.

(xi) The steps (iv) and (vi)–(x) are repeated iteratively.

This procedure converges after several iterations. The final empirical standard deviations  $\sigma_{\mu_{\alpha} \cos(\delta)}$  and  $\sigma_{\mu_{\delta}}$  appear reasonable, being slightly higher than the mean stated *Gaia* EDR3 PM uncertainties: 0.36 versus 0.29, 0.34 versus 0.25, and 0.35 versus 0.27 mas yr<sup>-1</sup> for NGC 288, NGC 362, and NGC 6218, respectively (averaged for the PM components).

The final truncation radii are 13.7, 18.7, and 14.9 arcmin for NGC 288, NGC 362, and NGC 6218, respectively. They are larger than those provided in Table 1 – 7.5, 7.5, and 9.5 arcmin, respectively. This increase of the radii adds 9, 19, and 7 per cent of members for NGC 288, NGC 362, and NGC 6218, respectively. However, they cannot be selected as cluster members without knowing their precise PMs. Anyway, these additional members do not change our results.

This cleaning is especially important for NGC 362 whose field is contaminated by SMC stars with different PMs. Fig. 3 shows the final distribution of stars, selected within 18.7 arcmin of the NGC 362 centre, by the proper motion components. A clear separation of the SMC and NGC 362 is evident. The  $3\sigma$  cut, shown by the red circles, seems to be reasonable. The CMD of these stars is shown in Fig. 4.

Since the stated *Gaia* EDR3 PM uncertainty strongly increases with magnitude, faint cluster members contribute negligibly to the weighted mean PMs.

Our final weighted mean PMs are presented in Table 5. They are compared with the estimates from VB21 and Vitral (2021), which are also based on *Gaia* EDR3. Despite different approaches used, these estimates are consistent within  $\pm 0.01$  mas yr<sup>-1</sup>. However, the *Gaia* EDR3 PM systematic errors may be higher, equally affecting all these estimates. The random uncertainty is indicated in Table 5 for our and Vitral (2021) estimates, while the total (random plus systematic) uncertainty – for those of VB21. VB21 find that these total uncertainty values should be considered as ‘the irreducible systematic floor’ on the accuracy of the *Gaia* EDR3 PMs ‘for any compact stellar system’, while 0.011 mas is a respective limit for its parallaxes. Hence, we adopt these values as the final uncertainties of our PMs, as well as of median parallaxes from *Gaia* EDR3. The latter are calculated by us with the parallax zero-point correction from *Gaia* Collaboration et al. (2021c) applied. We present these parallaxes in Table 1 and compare them with our results in Sect. 5.2.

Note that GC systemic PM estimates based on *Gaia* EDR3 are

most accurate to date. This is seen in their comparison with previous estimates of PMs, e.g. those recently obtained for NGC 362 by Libralato et al. (2018) using *HST* data:  $\mu_{\alpha} \cos(\delta) = 6.703 \pm 0.278$ ,  $\mu_{\delta} = -2.407 \pm 0.135$  mas yr<sup>-1</sup>.

The final lists of the *Gaia* EDR3 cluster members are presented in Table 6.

By use of the same approach, we select 5052 members of the SMC, which represent a background of NGC 362. They are presented in Fig. 3. We calculate their systemic PM:

$$\mu_{\alpha} \cos(\delta) = 0.786 \pm 0.004 \pm 0.026, \mu_{\delta} = -1.222 \pm 0.004 \pm 0.026$$

mas yr<sup>-1</sup>, where the former and latter errors are the random and systematic uncertainties, respectively. Note that due to the rotation of the SMC, this is the PM of a part of the SMC just behind NGC 362. Other parts may have a different PM.

To clean the SMSS datasets, we cross-identify them with the lists of the *Gaia* EDR3 members of these GCs and consider only common stars. This is an efficient and accurate segregation of the cluster members and contaminants, since both the SMSS and the *Gaia* EDR3 datasets are rather complete, deep and have many common stars.

#### 4 THEORETICAL MODELS AND ISOCHRONES

In order to fit the CMDs of NGC 288, NGC 362, and NGC 6218, we use the following theoretical models of stellar evolution and related pairs of  $\alpha$ -enhanced isochrones:

(i) BaSTI-IAC (Hidalgo et al. 2018; Pietrinferni et al. 2021) with  $[\text{Fe}/\text{H}] = -1.30$ ,  $[\alpha/\text{Fe}] = +0.40$ , initial solar  $Z_{\odot} = 0.0172$  and  $Y_{\odot} = 0.2695$ , overshooting, diffusion, mass loss efficiency  $\eta = 0.3$ , where  $\eta$  is the free parameter in Reimers law (Reimers 1975). We adopt  $Z = 0.001572$ ,  $Y = 0.249$  for primordial and  $Z = 0.001570$ ,  $Y = 0.275$  for helium-enriched population. The interpolated isochrone for  $Y = 0.26$  is between them. It is used to describe the observed mix of the populations. We also use the BaSTI-IAC extended set of zero-age horizontal branch (ZAHB) models with different values of the total mass but the same mass for the helium core and the same envelope chemical stratification. This set takes into account the assumption that stars with the same mass during the MS can lose different amount of mass during the RGB and, hence, differ in their colours and magnitudes during the HB. The BaSTI-IAC extended set of ZAHB models seems to be the most appropriate theoretical representation of the HB to date.

(ii) DSEP (Dotter et al. 2008) with  $[\text{Fe}/\text{H}] = -1.32$ ,  $[\alpha/\text{Fe}] = +0.40$ , solar  $Z_{\odot} = 0.0189$  and no mass loss. We use the isochrones with  $Z = 0.001564$ ,  $Y = 0.2475$  and  $Z = 0.001388$ ,  $Y = 0.33$ . DSEP provides no  $\alpha$ -enhanced isochrone for  $0.2475 < Y < 0.33$ . Therefore, we use the isochrone with  $Y = 0.2475$  to describe the primordial population, while interpolating in each CMD the isochrone with  $Y = 0.275$  for the helium-enriched population and the isochrone with  $Y = 0.26$  for a mix of the populations. Naturally, both the interpolated isochrones are much closer to that of  $Y = 0.2475$  than that of  $Y = 0.33$ . DSEP does not provide the HB and AGB.

DSEP and BaSTI-IAC are the only models providing  $\alpha$ -enhanced isochrones for almost all the filters under consideration. These models have demonstrated the most extreme results among all the models used in Paper I and Paper II: the lowest ages and the highest reddenings by DSEP, while the highest ages and the lowest reddenings by BaSTI-IAC. This can be explained if one compares the models in a diagram of effective temperature  $T_{\text{eff}}$  versus luminosity, i.e. before applying the colour– $T_{\text{eff}}$  relations and bolometric corrections. Such a



**Table 6.** The list of the *Gaia* EDR3 members of NGC 288, NGC 362, and NGC 6218. The complete table is available online.

NGC 288	NGC 362	NGC 6218
Gaia EDR3 2342707263271857664	Gaia EDR3 4690797804192972288	Gaia EDR3 4379051313863587968
Gaia EDR3 2342707267566820864	Gaia EDR3 4690797941632010624	Gaia EDR3 4379054165721868544
Gaia EDR3 2342712863909223168	Gaia EDR3 4690798010351505792	Gaia EDR3 4379054268801095296
Gaia EDR3 2342713070067644032	Gaia EDR3 4690809383424866560	Gaia EDR3 4379054513620043648
Gaia EDR3 2342713413665033600	Gaia EDR3 4690809795741849344	Gaia EDR3 4379054578038751232
...	...	...

comparison presented by Pietrinferni et al. (2021) or in figure 13 of Paper II shows that the DSEP RGB and TO are about 100 K hotter, while the DSEP SGB is slightly shorter than those of BaSTI-IAC. This is due to the differences in the physics inputs, most notably, in boundary conditions, solar metal mixture, and calibration of the solar standard model (Hidalgo et al. 2018; Pietrinferni et al. 2021). Note that DSEP and BaSTI-IAC show similar SGB luminosities and, consequently, provide nearly the same distances. Thus, DSEP and BaSTI-IAC are the most interesting models for our study. The diversity of all possible models should be covered by these two extreme models.

However, we have checked whether various solar-scaled models can substitute  $\alpha$ -enhanced ones as suggested by the rule of Salaris, Chieffi & Straniero (1993): ‘ $\alpha$ -enhanced isochrones are very well mimicked by the standard scaled solar isochrones of metallicity  $Z = Z_0(0.638f_\alpha + 0.362)$ , where  $f_\alpha$  is the chosen average enhancement factor of the  $\alpha$ -elements and  $Z_0$  is the initial (nonenhanced) metallicity’. For our GCs this means that solar-scaled isochrones with  $[\text{Fe}/\text{H}] \approx -1$  and  $\alpha$ -enhanced isochrones with  $[\text{Fe}/\text{H}] = -1.3$  would provide the same age, distance, and reddening. Pietrinferni et al. (2021) have found that the BaSTI-IAC isochrones for short wavelength filters significantly deviate from this rule. According to this, our testing of various models has not revealed a model following this rule in *all* the CMDs under consideration. Thus, we decide to use only DSEP and BaSTI-IAC  $\alpha$ -enhanced isochrones.

For *Gaia* DR2 and EDR3 we use isochrones based on the response curves of  $G$ ,  $G_{\text{BP}}$ , and  $G_{\text{RP}}$  from Gaia Collaboration et al. (2018) and Gaia Collaboration et al. (2021b), respectively.

We consider the isochrones for a grid of some reasonable distances with a step of 0.1 kpc, reddenings with a step of 0.001 mag, and ages over 8 Gyr with a step of 0.5 Gyr. Similar to Paper II, to derive the most probable reddening, distance, and age, we select an isochrone with a minimal total offset between the isochrone points and the fiducial points in the same magnitude range of the CMD.

## 5 RESULTS

Using this wealth of photometric data allows us to fit isochrones to dozens of CMDs with different colours. As in Paper I and Paper II, our results for different CMDs are consistent within their precision. Therefore, we show only some examples of the CMDs with isochrone fits in Figs 5–12<sup>16</sup>, while the derived ages, distances, and reddenings for NGC 288, NGC 362, and NGC 6218 are presented in Tables 7,

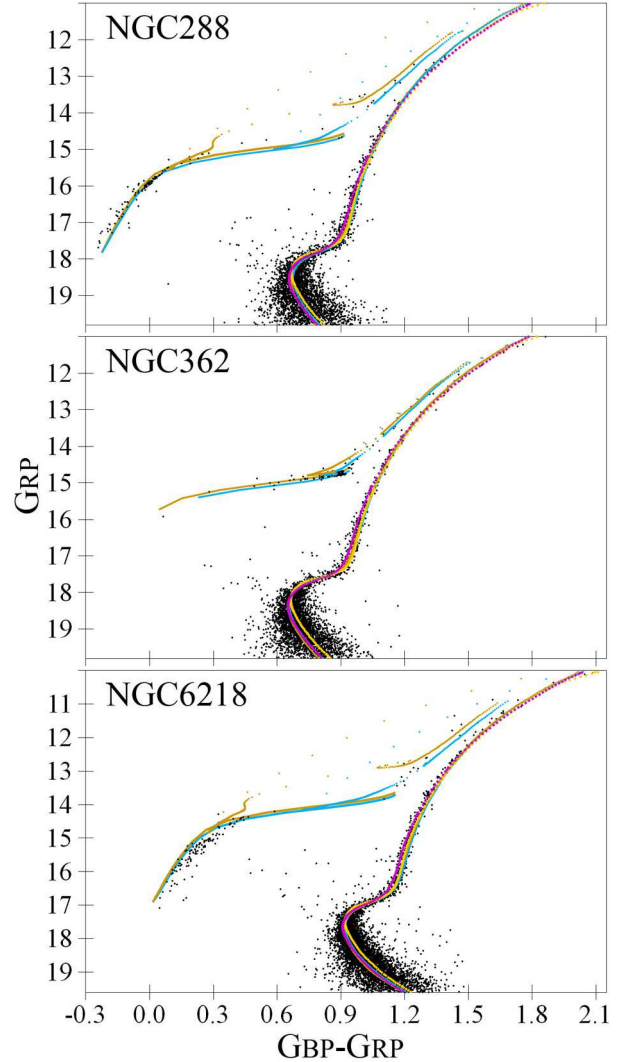


**Figure 5.** *Gaia* EDR3  $G_{\text{BP}} - G_{\text{RP}}$  versus  $G_{\text{RP}}$  CMD of NGC 288, NGC 362, and NGC 6218. The isochrones from BaSTI-IAC for  $Y = 0.249$  (blue) and  $0.275$  (brown) and from DSEP for  $Y = 0.2475$  (yellow) and  $0.33$  (purple) are calculated with the best-fitting parameters from Tables 7, 8, and 9, respectively. The DSEP isochrones are calculated for *Gaia* DR2, but they are shown here, since we find no significant systematic difference between the DR2 and EDR3 datasets.

<sup>16</sup> In all the CMDs, the colour is the abscissa and the magnitude in the redder filter is the ordinate.

**Table 7.** The results of the isochrone fitting for various models and some key colours for NGC 288. The complete table is available online. The *Gaia* DR2 results are shown for DSEP, while those from EDR3 – for BaSTI-IAC.

	DSEP	BaSTI-IAC
$E(G_{BP} - G_{RP})$ EDR3/DR2	$0.061 \pm 0.03$	$0.027 \pm 0.03$
age, Gyr	12.0	15.0
distance, kpc	9.0	8.8
$E(B - V)$ SPZ19	$0.012 \pm 0.02$	$-0.012 \pm 0.03$
age, Gyr	12.5	15.5
distance, kpc	9.1	8.9
$E(b - y)$	$0.022 \pm 0.02$	$0.005 \pm 0.02$
age, Gyr	12.5	14.5
distance, kpc	8.6	8.9
...	...	...

**Table 8.** The same as Table 7 but for NGC 362. The complete table is available online.

	DSEP	BaSTI-IAC
$E(G_{BP} - G_{RP})$ EDR3/DR2	$0.085 \pm 0.03$	$0.051 \pm 0.02$
age, Gyr	10.5	11.5
distance, kpc	8.6	8.8
$E(B - V)$ MCPS	$0.049 \pm 0.02$	$0.027 \pm 0.02$
age, Gyr	10.5	11.5
distance, kpc	8.8	9.0
$E(b - y)$	$0.040 \pm 0.03$	$0.026 \pm 0.03$
age, Gyr	10.0	10.5
distance, kpc	8.6	8.9
...	...	...

**Table 9.** The same as Table 7 but for NGC 6218. The complete table is available online.

	DSEP	BaSTI-IAC
$E(G_{BP} - G_{RP})$ EDR3/DR2	$0.295 \pm 0.03$	$0.268 \pm 0.02$
age, Gyr	13.0	15.5
distance, kpc	4.8	4.8
$E(B - V)$ SPZ19	$0.202 \pm 0.02$	$0.183 \pm 0.02$
age, Gyr	13.0	15.5
distance, kpc	4.8	4.8
$E(B - V)$ ZKR12	$0.204 \pm 0.02$	$0.190 \pm 0.02$
age, Gyr	12.5	14.0
distance, kpc	4.9	4.9
...	...	...

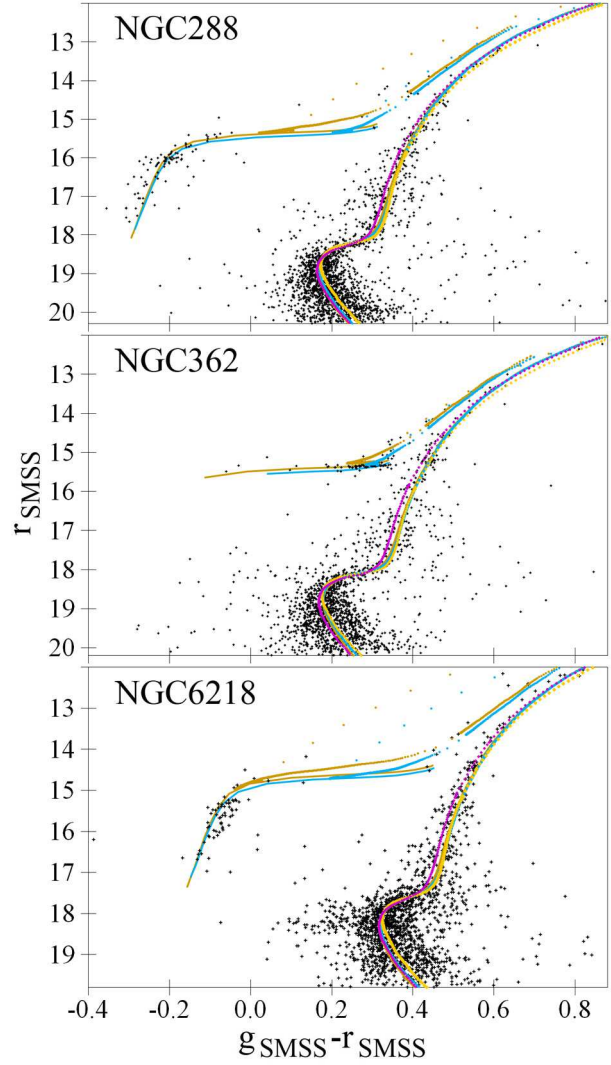


**Figure 6.** The same as Fig. 5 but for  $g_{SMSS} - r_{SMSS}$  versus  $r_{SMSS}$  CMD of NGC 288, NGC 362, and NGC 6218 based on the data from SMSS. The isochrones are calculated with the best-fitting parameters from Tables 7, 8, and 9, respectively.

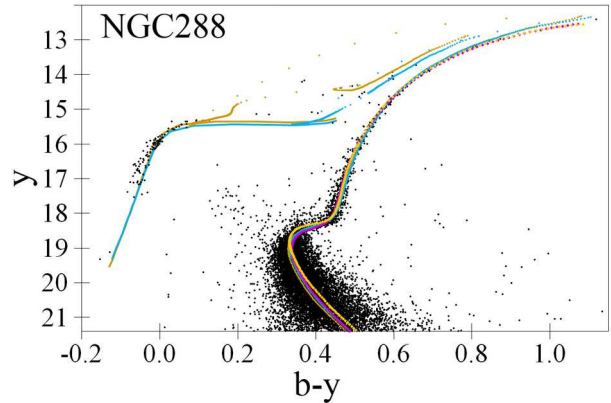


**Figure 7.** The same as Fig. 5 but for  $b - y$  versus  $y$  CMD of NGC 288 based on the data from GCL99. The isochrones are calculated with the best-fitting parameters from Table 7.

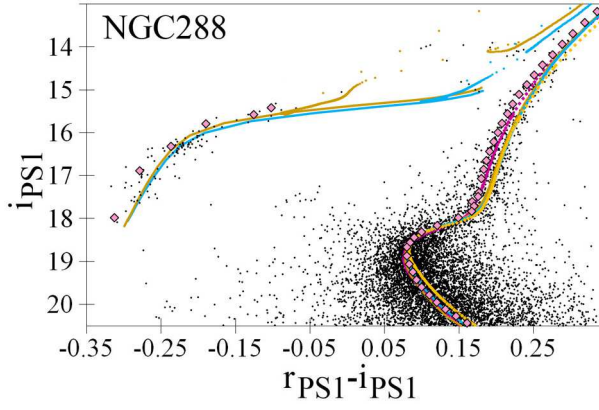


**Figure 8.** The same as Fig. 5 but for Pan-STARRS  $r_{PS1} - i_{PS1}$  versus  $i_{PS1}$  CMD of NGC 288 with the fiducial sequence of Bernard et al. (2014) shown as the pink diamonds. The isochrones are calculated with the best-fitting parameters from Table 7.

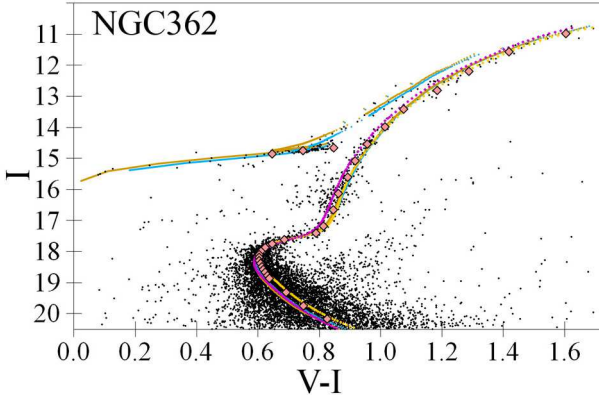


**Figure 9.** The same as Fig. 5 but for  $V - I$  versus  $I$  CMD of NGC 362 based on the data from BPF01 with their fiducial sequence shown as the pink diamonds. The isochrones are calculated with the best-fitting parameters from Table 8.

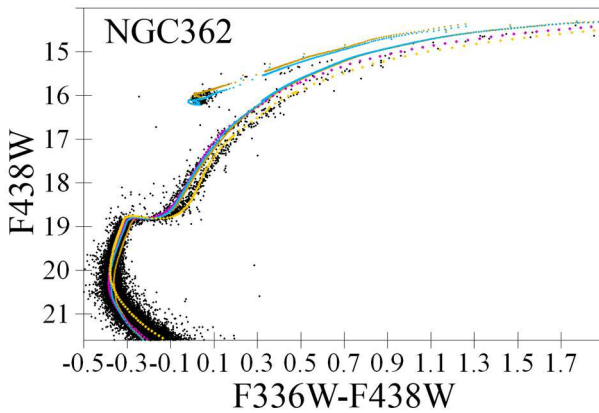


**Figure 10.** The same as Fig. 5 but for  $F336W - F438W$  versus  $F438W$  CMD of NGC 362 based on the *HST*/WFC3 data. The isochrones are calculated with the best-fitting parameters from Table 8.

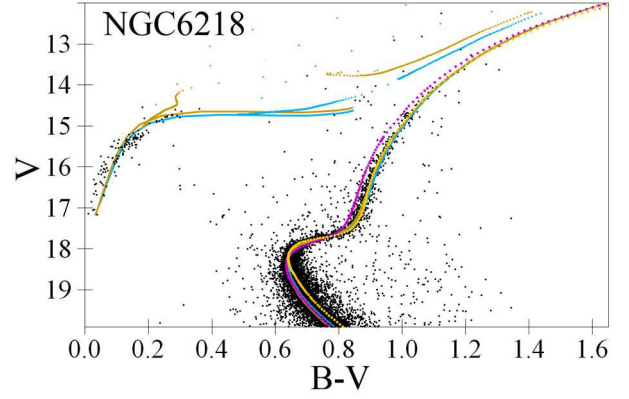


**Figure 11.** The same as Fig. 5 but for  $B - V$  versus  $V$  CMD of NGC 6218 based on the data from SPZ19. The isochrones are calculated with the best-fitting parameters from Table 9.

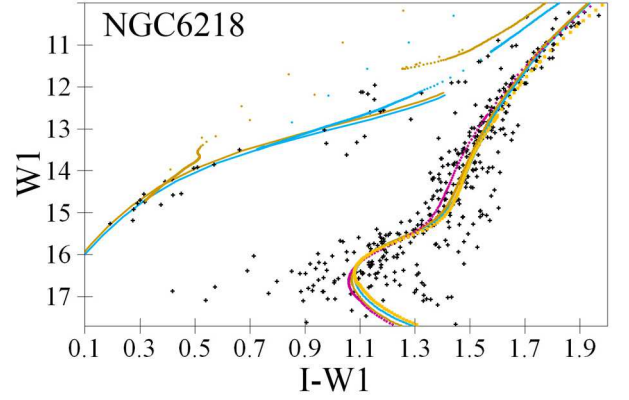


**Figure 12.** The same as Fig. 5 but for  $I - W1$  versus  $W1$  CMD of NGC 6218 based on the data from SPZ19 and unWISE. The isochrones are calculated with the best-fitting parameters from Table 9.

8, and 9, respectively. Figures for all the CMDs can be provided on request.

The isochrone fitting fails for some UV CMDs in this study, similar to NGC 6205 in Paper II. Hence, such UV CMDs are not presented in Tables 7–9 and not used for our final results.

In order to indicate the difference between the primordial and helium-enriched isochrones used, both the isochrones are shown in Figs 5–12. The interpolated isochrone for  $Y = 0.26$  is between them, as discussed in Sect. 4, and it is not shown for clarity. Thus, in Figs 5–12 we show four isochrones for the RGB, SGB, TO, and MS and two BaSTI-IAC isochrones for the HB and AGB. For most CMDs, especially for those in the optical range, the isochrone-to-fiducial fitting is so precise that the best-fitting isochrones of different models almost coincide with each other and with our fiducial sequence on the scales of our CMD figures for the RGB, SGB, and TO. Therefore, we do not show our fiducial sequences in Figs 5–12.

The following are notes on individual CMDs in Figs 5–12.

Fig. 5 presents the *Gaia* EDR3 dataset. It is about a magnitude deeper than that of *Gaia* DR2 and contains much more stars. We compare the magnitudes and colours of the common stars of the EDR3 and DR2 datasets and find no significant systematic difference. Therefore, we show both the BaSTI-IAC and DSEP isochrones in Fig. 5, although the former fits the *Gaia* EDR3 dataset, while the



latter – the *Gaia* DR2 dataset. An agreement of the BaSTI-IAC and DSEP isochrones is evident from Fig. 5.

Figs 5, 6, and some other CMDs show that:

- (i) The tip of the RGB is mainly populated by stars with the extreme helium enrichment (see Savino et al. 2018).
- (ii) There is a clear segregation of the two populations at the AGB for the old GCs (NGC 288 and NGC 6218).
- (iii) The BaSTI-IAC MS is too blue (Pietrinferni et al. 2021). This leads to a conflict between the two proxies of age, the SGB length and the HB–SGB magnitude difference: usually the former is too long w.r.t. the latter.
- (iv) There is a colour offset of the isochrones from the bluest HB stars of the old GCs. This offset cannot be eliminated by any reasonable variation of distance, age, or reddening. This offset can be explained by a special evolution of the bluest HB stars and/or by their unusual helium abundance (Heber 2016).
- (v) The length of the HB suggests the masses for the majority of the HB stars within  $0.54 - 0.62$ ,  $0.63 - 0.80$ , and  $0.54 - 0.62 M_{\odot}$  for NGC 288, NGC 362, and NGC 6218, respectively. However, both the *Gaia* EDR3 photometry in all three filters and SMSS photometry in the  $g_{SMSS}$ ,  $r_{SMSS}$ , and  $i_{SMSS}$  filters show few interesting marginals at the ZAHB: the reddest HB stars of NGC 288 with probable exceptionally high mass of  $0.78 M_{\odot}$  - *Gaia* EDR3 2342901537529620352 and *Gaia* EDR3 2342907992863854208, the bluest HB stars of NGC 362 with probable exceptionally low mass of  $0.6 M_{\odot}$  - *Gaia* EDR3 4690839418131927680 and *Gaia* EDR3 4690886353541485824, and the reddest HB stars of NGC 6218 with probable exceptionally high mass of  $0.72 M_{\odot}$  - *Gaia* EDR3 4379077294127099264 and *Gaia* EDR3 4379075984156919168. For the first time, very accurate *Gaia* EDR3 PMs ensure a very high probability for these stars to be cluster members. Properties of these marginals should be investigated in further studies.

Our cleaning of the datasets may differ from that fulfilled by their authors. Hence, our fiducial sequences may differ from those derived by the authors. For example, Fig. 8 shows that the fiducial sequence by Bernard et al. (2014) is a good representation of the MS and SGB of our sample, but is about 0.02 mag bluer than its RGB and HB. The reason for this discrepancy is a deeper cleaning of the Pan-STARRS dataset in our study. However, usually our fiducial sequence agrees with that derived by the dataset authors. An example is presented in Fig. 9: the fiducial sequence by BPF01 coincides with our fiducial sequence, which is not shown because it almost coincides with the best-fitting isochrones.

Fig. 10 shows a rare CMD with a significant colour difference [ $\Delta(F336W - F438W) \approx 0.07$  mag] between the populations at the RGB. This is a CMD for the UV filters. It is seen that two DSEP isochrones successfully fit the two observed RGBs. DSEP suggests that the primordial RGB population is redder than the helium-enriched one. Unlike DSEP, the BaSTI-IAC isochrones for the different populations almost coincide at the RGB. In such a case, both best-fitting isochrones should be exactly between the observed RGBs, if one takes into account the RGBs only. However, the best-fitting of the HB, AGB, SGB, and MS forces the best-fitting RGB isochrones to move blueward.

Fig. 12 shows a typical optical–IR CMD. Usually such a CMD contains less stars, more contaminants, and less pronounced HB and MS than an optical CMD. However, such a CMD still provides reliable distance, age and reddening estimates.

The predicted uncertainties of the derived distance, age, and reddening are very similar to those described in appendix A of Paper II. For a typical CMD these uncertainties are about 5 per cent, 7 per

cent and 0.03 mag for the derived distance, age, and reddening, respectively.

For each combination of a CMD/fiducial sequence and its best-fitting model/isochrone we find the maximal offset of this isochrone w.r.t. this fiducial sequence along the reddening vector (i.e. nearly along the colour). Such an offset is presented in Tables 7–9 after each value of reddening as its empirical uncertainty. We consider cases with an isochrone-to-fiducial offset greater than 0.15 mag as a fitting failure for the corresponding CMD.

For most CMDs, the predicted and empirical uncertainties are comparable. The largest value in such a pair of the uncertainties is shown by an error bar in Figs 13–15, which demonstrate the resulting extinction laws.

## 5.1 Reddening and extinction

Each CMD provides us with independent estimates of age, distance, and reddening. Each dataset in several filters, providing several CMDs, gives us an independent set of the derived reddenings. With such a set of reddenings, we can calculate the extinction for each filter of the dataset, if we adopt an extinction at the dataset filter with the longest wavelength, i.e. extinction zero-point.

Extinction and its uncertainty are minimal for IR filters. Therefore, we cross-identify each optical dataset with an IR dataset and adopt the extinction in an IR filter as the extinction zero-point for the optical dataset. The exceptions are made for three datasets, which cannot be cross-identified with an IR dataset and, hence, they have no IR extinction zero-point: the photometry from Piotto et al. (2002) and both the datasets represented by fiducial sequences only, without data for individual stars (Bolte 1992 and Davidge & Harris 1997).

Details on calculating extinctions and empirical extinction law are provided in section 5.1 of Paper II. Here we briefly summarise some important points: (i) we initially adopt any reasonable extinction in an IR filter used, (ii) we calculate extinctions in all the filters of the dataset by use of the corresponding reddenings and the IR extinction, (iii) the derived extinctions draw up an empirical extinction law for this specific dataset, (iv) we recalculate the IR extinction with the derived extinction law, and then repeat the steps (ii)–(iv) iteratively. We need only a few iterations to converge, since any reasonable variation of the extinction law results in a little variation of the IR extinction. For the clusters under consideration this variation is  $< 0.01$  mag.

We use the unWISE IR photometry for all the GCs, while for NGC 362 we also use the IR photometry from Cohen et al. (2015) and SAGE (except for BaSTI-IAC giving no SAGE isochrone). Both the  $J$  and  $K_s$  data from Cohen et al. (2015) are used in order to suppress possible systematics due to possible poor determination of the IR filter profiles.

Owing to the IR extinction zero-points, all the derived extinctions are rather precise being determined on a long UV–IR or optical–IR wavelength baseline. For example, we calculate

$$A_V = (A_V - A_{W1}) + A_{W1} = E(V - W1) + A_{W1} \quad (1)$$

from the reddening  $E(V - W1)$  and the IR extinction  $A_{W1}$ .

We adjust the datasets based on some CMDs obtained with pairs of filters from different datasets but of similar effective wavelengths. This adjustment follows its detailed description in section 6 of Paper II. We adjust magnitudes and colours from different datasets in order to minimise the scatter of extinctions from the datasets around an average extinction for each model. This adjustment does



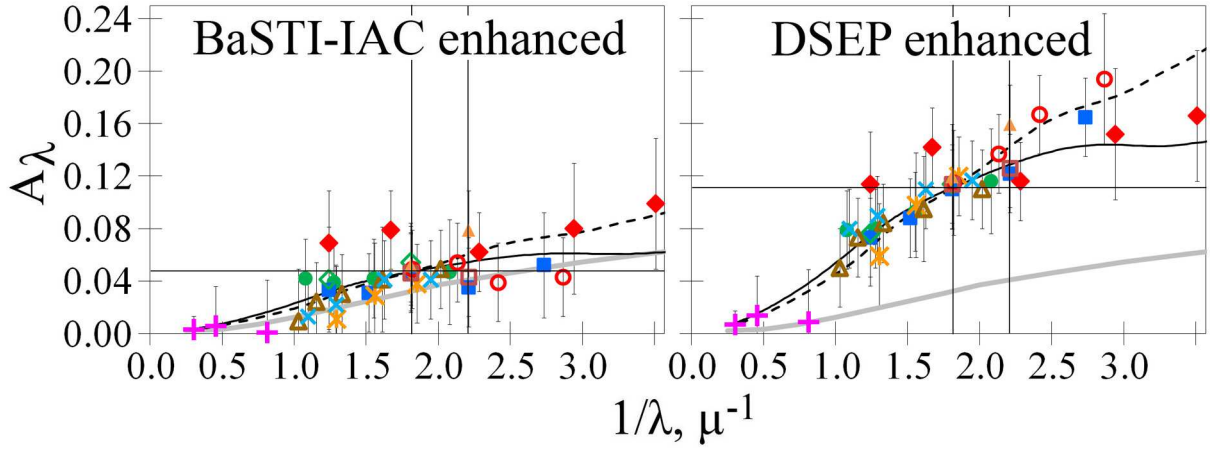


**Figure 13.** The empirical extinction laws for NGC 288 from the isochrone fitting by the different models. The datasets are: *HST* ACS and WFC3 by Nardiello et al. (2018) – red diamonds; *Gaia* – yellow snowflakes; SPZ19 – blue squares; BPF01 – open green diamonds; Bolte (1992) – yellow triangles; SFL16 – open brown squares; GCL99 – open red circles; Pan-STARRS – open brown triangles; DES – green circles; SMSS – blue inclined crosses; IR datasets by Davidge & Harris (1997) and unWISE – purple upright crosses. For the *B* and *V* filters, which are denoted by the vertical lines, the symbols are almost overlapping. The thick grey curve shows the extinction law of Schlafly et al. (2016) with  $A_V = 0.033$  mag. The black dotted and solid curves show the extinction law of CCM89 with  $R_V = 3.1$  and  $5.7$ , respectively, with the derived  $A_V$ , which is shown by the horizontal line.

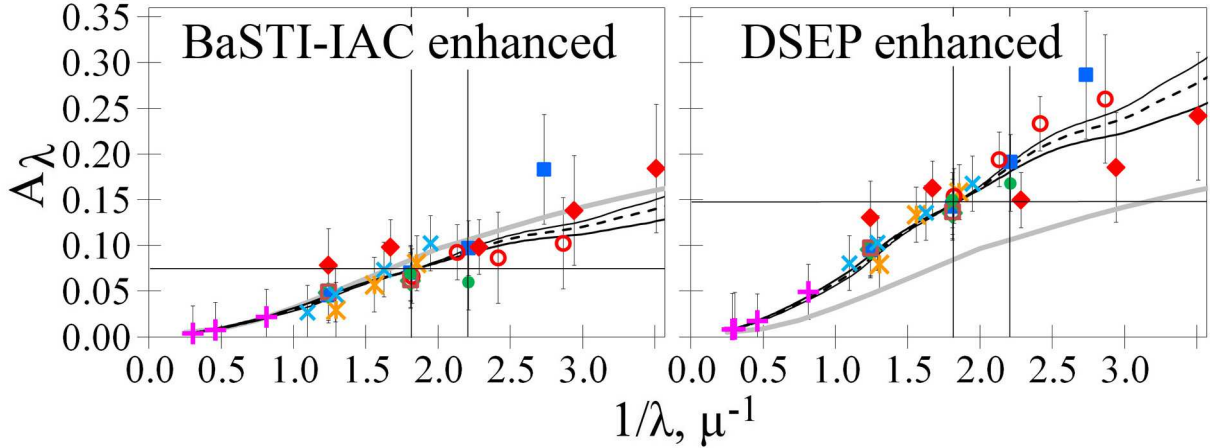


**Figure 14.** The same as Fig. 13 but for NGC 362. The datasets are: *HST* ACS and WFC3 – red diamonds; *HST* WFPC2 by Piotto et al. (2002) – green circles; *Gaia* – yellow snowflakes; MCPS – blue squares; BPF01 – open green diamonds; RPS00 – open brown squares; GCL99 – open red circles; SMSS – blue inclined crosses; IR datasets by Cohen et al. (2015), unWISE, and SAGE – purple upright crosses. For the *B* and *V* filters, which are denoted by the vertical lines, the symbols are almost overlapping. The thick grey curve shows the extinction law of Schlafly et al. (2016) with  $A_V = 0.086$  mag. The black thin, dotted and thick curves show the extinction law of CCM89 with  $R_V = 2.8, 3.1$  and  $3.6$ , respectively, with the derived  $A_V$ , which is shown by the horizontal line.

not change the average extinctions, distances, and ages derived for each model. All the adjustment corrections are within  $\pm 0.035$  mag<sup>17</sup>.

The adjustment corrections to the same model–dataset pair (such as BaSTI-IAC–*Gaia* EDR3) appear slightly different for different GCs. Hence, they may be due to some systematic errors of the datasets, which vary from one GC to another with observational conditions, celestial position, or time (see a detailed analysis by Anderson et al. 2008).

Some datasets cannot be adjusted since they have no appropriate filters, or they have little, if any, common stars with the other datasets. An example is the *HST* ACS/WFC3 datasets of Nardiello et al.

(2018). They provide a systematically higher extinction (red diamonds in Figs 13–15) w.r.t. the other datasets. However, the *HST* ACS/WFC3 datasets are not adjusted w.r.t. the other datasets, since the former are obtained within approximately 2 arcmin from the cluster centres, where the other datasets have little stars. Therefore, we cannot make a final conclusion about the reason for this deviation of the *HST* ACS/WFC3 extinction estimates. This may be due to some systematic errors of these datasets or due to a population variation in the cluster centres. This deviation of the *HST* ACS/WFC3 extinction estimates needs further study.

The extinction  $A_V$  requires special attention, since we have a wealth of data to determine it. Moreover, we can use some datasets without the *V* filter to validate the average system obtained for the datasets with the *BVI* filters. The derived extinctions  $A_V$  are presented in Tables 10, 11, and 12 for NGC 288, NGC 362, and NGC 6218, respectively. In these tables, the datasets, listed in the

<sup>17</sup> The unWISE–SAGE  $W1 - 3.6 \mu\text{m}$  colour differences for the common NGC 362 stars show that the DSEP predictions for SAGE should be corrected by  $+0.12$  mag.

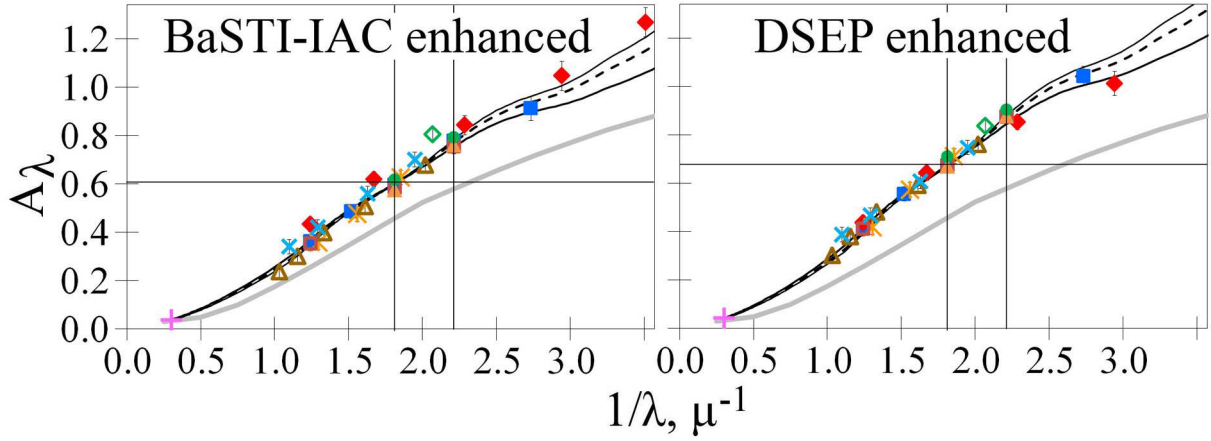


**Figure 15.** The same as Fig. 13 but for NGC 6218. The datasets are: *HST* ACS and WFC3 by Nardiello et al. (2018) – red diamonds; *HST* ACS by Simioni et al. (2018) – open green diamonds; *HST* WFPC2 by Piotto et al. (2002) – green circles; *Gaia* – yellow snowflakes; *SPZ19* – blue squares; *ZKR12* – yellow triangles; *HSB04* – open brown squares; Pan-STARRS – open brown triangles; SMSS – blue inclined crosses; unWISE – purple upright crosses. For the *B* and *V* filters, which are denoted by the vertical lines, the symbols are almost overlapping. The thick grey curve shows the extinction law of Schlafly et al. (2016) with  $A_V = 0.467$  mag. The black thin, dotted and thick curves show the extinction law of CCM89 with  $R_V = 2.9, 3.1$  and  $3.5$ , respectively, with the derived  $A_V$ , which is shown by the horizontal line. The error bars are typically shorter than the size of the symbols used.

**Table 10.** The estimates of  $A_V$  for NGC 288 from the various datasets and models.

Model	Dataset	
	SPZ19, GCL99, BPF01, SFL16	The same plus <i>HST</i> , PS1, DES, <i>Gaia</i> , and SMSS
BaSTI-IAC enhanced	$0.049 \pm 0.004$	$0.047 \pm 0.009$
DSEP enhanced	$0.112 \pm 0.003$	$0.111 \pm 0.006$
Mid-range value	$0.080 \pm 0.032$	$0.079 \pm 0.032$

**Table 11.** The estimates of  $A_V$  for NGC 362 from the various datasets and models.

Model	Dataset	
	MCPS, GCL99, RPS00, BPF01	The same plus <i>HST</i> and <i>Gaia</i>
BaSTI-IAC enhanced	$0.065 \pm 0.005$	$0.073 \pm 0.011$
DSEP enhanced	$0.142 \pm 0.009$	$0.146 \pm 0.010$
Mid-range value	$0.104 \pm 0.039$	$0.109 \pm 0.037$

**Table 12.** The estimates of  $A_V$  for NGC 6218 from the various datasets and models.

Model	Dataset	
	SPZ19, ZKR12, HSB04	The same plus <i>HST</i> , Pan-STARRS, and <i>Gaia</i>
BaSTI-IAC enhanced	$0.583 \pm 0.009$	$0.600 \pm 0.029$
DSEP enhanced	$0.659 \pm 0.019$	$0.668 \pm 0.017$
Mid-range value	$0.621 \pm 0.038$	$0.634 \pm 0.034$

central column, allow a direct determination of  $A_V$  by use of eq. (1) or a similar equation for another IR filter, without knowledge of the extinction law. In the rightmost column we present the results obtained with these and some additional datasets. Each additional dataset includes several filters and has an IR extinction zero-point, but it provides no direct determination of  $A_V$ . In this case, we calculate  $A_V$  from the extinction in adjacent filters by use of the following extinction law relations:

- (i)  $A_V = 0.53(A_{G_{BP}} + A_G)$  for *Gaia*,
- (ii)  $A_V = 0.49(A_{g_{DECam}} + A_{r_{DECam}})$  for DES,
- (iii)  $A_V = 0.50(A_{g_{PS1}} + A_{r_{PS1}})$  for Pan-STARRS,
- (iv)  $A_V = 0.44(A_{F438W} + A_{F606W})$  for *HST*, and
- (v)  $A_V = 0.51(A_{g_{SMSS}} + A_{r_{SMSS}})$  for SMSS.

The coefficients in these relations are rather close to 0.5, since we use the pairs of filters, which are rather close and nearly symmetric in wavelength w.r.t. the  $V$  filter. These coefficients vary only within  $\pm 0.015$  for the extinction laws of Fitzpatrick (1999), Schlafly et al. (2016), Wang & Chen (2019), and CCM89 with  $2.4 < R_V < 4.1$ . Therefore, the use of these coefficients without knowing the proper extinction law provides a relative uncertainty of the obtained  $A_V$  of less than  $0.015/0.44 = 0.034$  and, hence, a negligible contribution of  $\pm 0.004$ ,  $\pm 0.004$ , and  $\pm 0.02$  mag to the final  $A_V$  uncertainty in Tables 10–12.

The  $A_V$  estimates in Tables 10–12 agree for the different datasets (i.e. those in the central and rightmost columns). Hereafter, we prefer the values obtained for the larger lists of the datasets.

However, the  $A_V$  estimates in Tables 10–12 disagree for the different models (i.e. those in different rows). This disagreement seems to be due to a systematic difference between the models. We decide to calculate our final estimates as the mid-range (a middle value between the model estimates) values<sup>18</sup> with their uncertainties as half the differences between the DSEP and BaSTI-IAC estimates:  $A_V = 0.08 \pm 0.03$ ,  $0.11 \pm 0.04$ , and  $0.63 \pm 0.03$  mag for NGC 288, NGC 362, and NGC 6218, respectively.

Following Tables 10–12, Figs 13–15 show a low scatter for the datasets, while a large difference between the models.

Our  $A_V$  estimates for NGC 288 and NGC 6218 are considerably higher than those in Table 1 from the 2D dust emission maps of Schlegel, Finkbeiner & Davis (1998), Schlafly & Finkbeiner (2011), and Meisner & Finkbeiner (2015). This is also seen in Figs 13–15 where the thick grey curves show the extinction law of Schlafly et al. (2016) with the extinction estimate from Schlafly & Finkbeiner (2011): DSEP for all the GCs and both the models for NGC 6218 provide the empirical extinction laws, which cannot be reconciled with the prediction of Schlafly & Finkbeiner (2011).

However, our  $A_V$  estimates are lower than those from Wagner-Kaiser et al. (2016, 2017), who used a Bayesian single- and two-population analysis for the *HST* ACS data and obtained  $0.084 < A_V < 0.140$ ,  $0.117 < A_V < 0.128$ , and  $0.682 < A_V < 0.695$  for NGC 288, NGC 362, and NGC 6218, respectively.

This wide spread of the  $A_V$  estimates from the literature may be due to the incorrect extinction-to-reddening coefficients used. Usually, an extinction estimate is extrapolated from a reddening, measured in a narrow wavelength range, by use of an adopted extinction law. If such a law differs from the proper law, this introduces an additional

extrapolation error. The most common way (giving all the estimates of the 2D maps in Table 1) has been the extrapolation of the observed reddening  $E(B - V)$  to  $A_V$ . Therefore, it is interesting to calculate and compare  $E(B - V)$  estimates for these GCs.

To estimate  $E(B - V)$  from Tables 7–9, we use both the  $E(B - V)$  estimates themselves and the  $E(b - y)$  reddenings in the adjacent Strömgren  $b$  and  $y$  filters by use of the extinction law relation  $E(B - V) = 1.29E(b - y)$ <sup>19</sup>. Since this pair of filters is rather close and nearly symmetric in wavelength w.r.t. the  $BV$  pair, the coefficient in this relation varies negligibly (only within  $\pm 0.01$ ) for the extinction laws of Fitzpatrick (1999), Schlafly et al. (2016), Wang & Chen (2019), and CCM89 with  $2.3 < R_V < 4.0$ .

We obtain  $E(B - V) = 0.014 \pm 0.010$ ,  $0.028 \pm 0.011$ , and  $0.189 \pm 0.010$  mag for NGC 288, NGC 362, and NGC 6218, respectively. Similar to the  $A_V$  estimates, the DSEP and BaSTI-IAC  $E(B - V)$  estimates differ significantly. Hence, these uncertainties are half the differences between the model estimates. These  $E(B - V)$  estimates for NGC 288 and NGC 362 are about their lowest reddening estimates in Table 1. In combination with rather high  $A_V$  estimates, this suggests that the observed extinction law may deviate from the laws adopted for the estimates in Table 1. This is seen in Figs 13 and 14 with the empirical extinction laws for NGC 288 and NGC 362, respectively: all the data in the  $BV$  range show little increase of extinction with the wavelength.

Given our estimates of  $A_V$  and  $E(B - V)$  with their uncertainties, our estimates of  $R_V$  from the different models are consistent, although they are poorly constrained for NGC 288 and NGC 362:  $R_V > 3.1$  for NGC 288,  $R_V > 2.1$  for NGC 362, and  $R_V = 3.35^{+0.25}_{-0.23}$  for NGC 6218. We emphasise that these  $R_V$  estimates characterise the empirical extinction law only between the  $B$  and  $V$  filters. Alternatively,  $R_V$  for the whole wavelength range under consideration can be estimated from the derived extinctions in all the filters of all the datasets, separately for each model. This is the  $R_V$  estimate, which we use to calculate the IR extinction zero-points mentioned above. In Figs 13–15 we depict the CCM89 extinction law with the derived  $A_V$  and various  $R_V$  shown by the black curves. Taking the error bars into account, all our results are in acceptable agreement with the common CCM89 extinction law with  $R_V = 3.1$ , which is shown by the dotted curve. Hence, we adopt this law to calculate the IR extinction zero-points. However, Figs 13–15 show that the empirical extinction law can be better presented by the CCM89 law with  $3.1 < R_V < 5.7$ ,  $2.8 < R_V < 3.6$ , and  $2.9 < R_V < 3.5$  for NGC 288, NGC 362, and NGC 6218, respectively.

Paper II has shown that all most reliable extinction laws, such as those of Fitzpatrick (1999), Schlafly et al. (2016), and Wang & Chen (2019), with the same  $A_V$  are very close to the CCM89 extinction law and to each other. Therefore, the choice of law or  $R_V$  can barely change the agreement of a law with our results in Figs 13–15, but the choice of  $A_V$  can. Thus, we emphasise that Tables 10–12 contain our most important results about extinction for these GCs.

The reddening or extinction estimates from Schlegel, Finkbeiner & Davis (1998), Schlafly & Finkbeiner (2011), and Meisner & Finkbeiner (2015) in Table 1 are most frequently used in studies of extragalactic objects at middle

<sup>18</sup> Here the mid-range values are equal to the mean values. However, we entitle designate the bottom rows of Tables 10–12 as mid-range values in order to emphasise that their uncertainties are not standard deviations but half the differences between the DSEP and BaSTI-IAC estimates.

<sup>19</sup> *HST* WFC3 *F*438W and ACS *F*606W filter pair also may be a good proxy of the  $B$  and  $V$  filters. However, belonging to the different detectors (WFC3 and ACS), these filters may allow a small instrumental systematic error in the  $F438W - F606W$  colour. Even being 0.01 mag, such an error significantly affects very small reddening  $E(F438W - F606W)$  of NGC 288 and NGC 362. Therefore, we decide not to use  $E(F438W - F606W)$  in our  $E(B - V)$  calculation.

and high Galactic latitudes. A possible underestimation of low extinctions by these studies has been found by various methods (Gontcharov & Mosenkov 2017a,b, 2018, 2021), in particular, in Paper I and Paper II for both NGC 5904 and NGC 6205. However, this study shows that this issue is even more complex, when extinction is underestimated while reddening is overestimated by these maps for some GCs. This suggests that a proper extinction law differs from an adopted law. In the case of an uncertain proper extinction law, we recommend to use extinction instead of reddening, since extinction is valid on a longer wavelength baseline.

## 5.2 Age and distance

Our age and distance estimates for NGC 288, NGC 362, and NGC 6218 are presented in Tables 13, 14, and 15, respectively. Their uncertainties are standard deviations calculated from all reliable independent CMDs with the given model applied.

We separate the results for the optical range ( $0.42 < \lambda < 1.0$  nm) and the UV and IR ranges. Similar to NGC 6205 in Paper II, the results for the ranges differ, both systematically and by their standard deviations. Assuming that the models are more accurate in the optical range, we decide to use the estimates in the optical range as the final, most probable estimates.

The right column presents the mean value and standard deviation of the combined results for the two models. It is seen that the models provide consistent estimates of distance, but inconsistent estimates of age. Therefore, we accept the final uncertainty of our distance estimates as the standard deviation of the combined sample divided by the square root of the number of the CMDs used. In contrast, we accept the final uncertainty of our age estimates as half the difference between the model estimates.

Our final estimates for NGC 288, NGC 362, and NGC 6218, respectively, are:

- (i) age is  $13.5 \pm 1.1$ ,  $11.0 \pm 0.6$ , and  $13.8 \pm 1.1$  Gyr,
- (ii) distance is  $8.96 \pm 0.05$ ,  $8.98 \pm 0.06$ , and  $5.04 \pm 0.05$  kpc,
- (iii) distance modulus  $(m - M)_0$  is  $14.76 \pm 0.01$ ,  $14.77 \pm 0.01$ , and  $13.51 \pm 0.02$  mag,
- (iv) apparent  $V$ -band distance modulus  $(m - M)_V$  is  $14.84 \pm 0.03$ ,  $14.88 \pm 0.04$ , and  $14.14 \pm 0.04$  mag.

Our distance estimates agree with those from the recent compilation of all distance determinations by Baumgardt & Vasiliev (2021) within  $0.2\sigma$ ,  $0.9\sigma$ , and  $0.7\sigma$  of the stated uncertainties for NGC 288, NGC 362, and NGC 6218, respectively. It is worth noting that other studies in the compilation of Baumgardt & Vasiliev (2021) have considered only one or a few datasets, while in our paper a dozen of datasets for each cluster is analysed in detail. Therefore, our distance estimates for these clusters should be among most accurate.

Our distances correspond to the parallaxes  $0.1116 \pm 0.0006$ ,  $0.1114 \pm 0.0008$ , and  $0.1984 \pm 0.0020$  mas for NGC 288, NGC 362, and NGC 6218, respectively. They agree within their uncertainties with the median corrected *Gaia* EDR3 parallaxes, which we obtain in Sect. 3.2 and present in Table 1:  $0.114 \pm 0.011$ ,  $0.119 \pm 0.011$ , and  $0.210 \pm 0.011$  mas for NGC 288, NGC 362, and NGC 6218, respectively. However, all the *Gaia* EDR3 parallaxes are higher than ours. This comparison confirms the conclusion of VB21 that the corrected *Gaia* EDR3 parallaxes are overestimated by  $\sim 0.006 - 0.009$  mas. Anyway, it is evident that the GC distances from the *Gaia* EDR3 parallaxes are still less accurate than those obtained from such an isochrone fitting.

Our age estimates are within a wide variety of age estimates

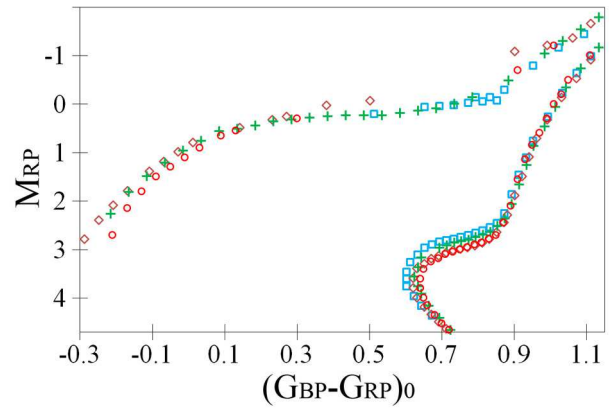


**Figure 16.** The CMD with the *Gaia* EDR3 fiducial sequences for NGC 288 (brown diamonds), NGC 362 (blue squares), NGC 5904 (green crosses), and NGC 6218 (red circles).

for these GCs from the literature<sup>20</sup>. For example, our age estimates are in acceptable agreement with that of  $11.5 \pm 2.0$  Gyr for NGC 288 from O'Malley, Gilligan & Chaboyer (2017), as well as with the age estimates from the isochrone fitting of the *HST* ACS data<sup>21</sup> by VandenBerg et al. (2013):  $11.50 \pm 0.38$ ,  $10.75 \pm 0.25$ , and  $13.00 \pm 0.50$  Gyr for NGC 288, NGC 362, and NGC 6218, respectively. This age estimate for NGC 288 is much younger than ours. However, VandenBerg et al. (2013) note for NGC 288 'Both the slope of the SGB and the location of the RGB are less problematic if the higher age is assumed.'

Our age estimates agree with those from the Bayesian single-population analysis of the same *HST* ACS data by Wagner-Kaiser et al. (2017):  $13.50 \pm 0.01$ ,  $11.46 \pm 0.10$ , and  $13.50 \pm 0.01$  Gyr for NGC 288, NGC 362, and NGC 6218, respectively. However, our estimates are much less consistent with those from the two-population analysis of the same data by Wagner-Kaiser et al. (2016):  $11.03 \pm 0.04$ ,  $9.99 \pm 0.02$ , and  $12.88 \pm 0.02$  Gyr for NGC 288, NGC 362, and NGC 6218, respectively. This may be explained by the fact that two populations of these GCs are not segregated in the  $F606W - F814W$  CMD (VandenBerg et al. 2013). Hence, a two-population analysis seems to be less appropriate in this case.

The models are consistent in their relative age estimates: NGC 362 is  $2.6 \pm 0.5$  Gyr younger than NGC 288 and  $2.8 \pm 0.5$  Gyr younger than NGC 6218<sup>22</sup>. These estimates are the mean differences between the age estimates in Tables 13–15, computed separately for each model. The uncertainties are half the differences between the model estimates. Following the balance of uncertainties in appendix A of Paper II, we note that, in the case of a relative age calculation, the uncertainties of model, colour- $T_{\text{eff}}$  relation and bolometric correction are not important. Hence, photometric errors (decreased by our use of several datasets) and an uncertainty due to multiple populations dominate uncertainty of the final relative age. This explains the much lower uncertainties of the relative ages w.r.t. those of the absolute ages.

NGC 5904 has a similar metallicity. Our age estimate  $12.15 \pm 1.0$  Gyr for NGC 5904 from Paper I suggests that it is 1.15 Gyr older than NGC 362. Thus, one can see a clear correlation of the derived relative

<sup>20</sup> This variety is a reason why there is no consensus about age as the second parameter.

<sup>21</sup> We use the same photometry in the  $F606W$  and  $F814W$  filters.

<sup>22</sup> These estimates agree with some previous ones, e.g. by BPF01.



**Table 13.** Our age (Gyr) and distance (kpc) estimates for NGC 288.

	DSEP	BaSTI-IAC	Mean value
Mean distance for $0.42 < \lambda < 1.0$ nm	$9.04 \pm 0.23$	$8.89 \pm 0.16$	$8.96 \pm 0.21$
Mean distance for the UV and IR range	$8.78 \pm 0.41$	$8.79 \pm 0.32$	$8.79 \pm 0.36$
Mean age for $0.42 < \lambda < 1.0$ nm	$12.45 \pm 0.60$	$14.63 \pm 0.92$	$13.54 \pm 1.34$
Mean age for the UV and IR range	$12.53 \pm 0.78$	$13.81 \pm 0.85$	$13.17 \pm 1.04$

**Table 14.** Our age (Gyr) and distance (kpc) estimates for NGC 362.

	DSEP	BaSTI-IAC	Mean value
Mean distance for $0.42 < \lambda < 1.0$ nm	$8.95 \pm 0.27$	$9.02 \pm 0.13$	$8.98 \pm 0.21$
Mean distance for the UV and IR range	$8.86 \pm 0.34$	$8.99 \pm 0.21$	$8.92 \pm 0.29$
Mean age for $0.42 < \lambda < 1.0$ nm	$10.42 \pm 0.47$	$11.54 \pm 0.54$	$10.98 \pm 0.76$
Mean age for the UV and IR range	$10.63 \pm 1.16$	$11.22 \pm 0.93$	$10.89 \pm 1.10$

**Table 15.** Our age (Gyr) and distance (kpc) estimates for NGC 6218.

	DSEP	BaSTI-IAC	Mean value
Mean distance for $0.42 < \lambda < 1.0$ nm	$5.09 \pm 0.24$	$5.00 \pm 0.17$	$5.04 \pm 0.21$
Mean distance for the UV and IR range	$5.11 \pm 0.19$	$5.12 \pm 0.19$	$5.11 \pm 0.18$
Mean age for $0.42 < \lambda < 1.0$ nm	$12.75 \pm 0.73$	$14.89 \pm 0.99$	$13.82 \pm 1.38$
Mean age for the UV and IR range	$13.25 \pm 0.72$	$14.14 \pm 0.78$	$13.71 \pm 0.86$

ages with the HB type<sup>23</sup> +0.98, −0.87, +0.31, and +0.98 taken from VandenBerg et al. (2013) for NGC 288, NGC 362, NGC 5904, and NGC 6218, respectively. This is an important result. Since we use by far the most expanded data, our result is a robust confirmation of the long-standing assumption that age is the second parameter for these GCs.

A direct comparison of the HBs and SGBs of these GCs is useful. Table 2 shows that *HST* ACS/WFC3, *Gaia*, and SMSS are the only common datasets for these GCs. However, the *HST* dataset covers only a few central arcminutes of the fields and shows the unexplained extinction deviation, as noted in Sect. 5.1. *Gaia* EDR3 contains more stars and better defined fiducial sequences than SMSS. Therefore, we compare the HBs in the *Gaia* EDR3 CMD. We transfer our *Gaia* EDR3 fiducial sequences into the plane of the dereddened colour  $(G_{BP} - G_{RP})_0$  versus the absolute magnitude  $M_{GRP}$  by use of the reddenings and distances from Tables 7–9 and the CCM89 extinction law. Also, we process the *Gaia* EDR3 data of NGC 5904, obtain its fiducial sequence, and transfer it by use of the reddening and distance from Paper I. The fiducial sequences of the four GCs

are shown in Fig. 16 by different open symbols. The RGB colours of the different fiducial sequences coincide within  $\pm 0.01$  mag. Good agreement between their HB magnitudes within  $\pm 0.05$  mag is evident, if we compare them w.r.t. the HB of NGC 5904, which spans the whole colour range. This good agreement<sup>24</sup> for the RGBs and HBs of the different fiducial sequences means that we adopt the correct reddenings (important for positioning RGBs) and correct distances (important for positioning HBs).

A small colour offset between the bluest HB fiducial sequence points of NGC 288, NGC 5904, and NGC 6218 remains. This offset cannot be eliminated, when the HBs and RGBs are fixed (see our discussion of Figs 5 and 6).

Fig. 16 shows that in the sequence NGC 362, NGC 5904, NGC 288, and NGC 6218, the HB–SGB magnitude difference increases, while the SGB length decreases. Thus, we can infer that the age of the clusters in this sequence increases. On the other hand, the HB morphology also changes along this sequence: NGC 362 has only a red HB, the HB of NGC 5904 spans the whole colour range, while NGC 288 and NGC 6218 have only a blue HB. Therefore, this correlation of

<sup>23</sup> The HB type is defined as  $(N_B - N_R)/(N_B + N_V + N_R)$ , where  $N_B$ ,  $N_V$ , and  $N_R$  are the number of stars that lie blueward of the instability strip, the number of RR Lyrae variables, and the number of stars that lie redward of the instability strip, respectively (Lee, Demarque & Zinn 1994).

<sup>24</sup> This agreement is sufficient to see the various HB–SGB magnitude differences for these GCs. We ensure the final agreement by use of several datasets.

the morphology with the HB–SGB magnitude difference and SGB length strongly suggests the morphology variation with age.

## 6 CONCLUSIONS

This study generally follows [Paper I](#) and [Paper II](#) in their approach to estimate distance, age, and extinction law of Galactic GCs by fitting model isochrones to a multiband photometry. We have considered the famous second-parameter pair NGC 288 and NGC 362 with a very low extinction, as well as the middle-latitude cluster NGC 6218 (M12) of nearly the same metallicity. For all three clusters, we accepted the metallicity  $[\text{Fe}/\text{H}] = -1.3$  based on the spectroscopy taken from the literature.

We used the photometry of the clusters in many filters from the *HST*, *unWISE*, *Gaia* DR2 and EDR3, Pan-STARRS, SkyMapper Southern Sky Survey DR3 and other datasets. These filters cover a wavelength range from about 235 to 4070 nm, i.e. from the UV to mid-IR. Some of the photometric datasets were cross-identified with each other. This allowed us (i) to use an IR photometry with a nearly zero extinction for accurate determination of extinction in all other filters and (ii) to estimate some systematic differences of the datasets and suppress them to a level of  $< 0.01$  mag.

To fit the data, we used the DSEP and BaSTI-IAC theoretical models of the stellar evolution for  $\alpha$ -enhanced populations of the GCs with different helium abundance. An improvement of these models in recent years makes isochrone-to-data fitting in a typical optical CMD fairly precise. However, the models are still inconsistent in their predictions for age and reddening.

For NGC 288, NGC 362, and NGC 6218, we derived the most probable distances  $8.96 \pm 0.05$ ,  $8.98 \pm 0.06$ , and  $5.04 \pm 0.05$  kpc, distance moduli  $14.76 \pm 0.01$ ,  $14.77 \pm 0.01$ , and  $13.51 \pm 0.02$  mag, apparent *V*-band distance moduli  $14.84 \pm 0.03$ ,  $14.88 \pm 0.04$ , and  $14.14 \pm 0.04$  mag, ages  $13.5 \pm 1.1$ ,  $11.0 \pm 0.6$ , and  $13.8 \pm 1.1$  Gyr, extinctions  $A_V = 0.08 \pm 0.03$ ,  $0.11 \pm 0.04$ , and  $0.63 \pm 0.03$  mag, and reddenings  $E(B - V) = 0.014 \pm 0.010$ ,  $0.028 \pm 0.011$ , and  $0.189 \pm 0.010$  mag, respectively. This leads to  $R_V = 3.35^{+0.25}_{-0.23}$  for NGC 6218. The extinction laws for NGC 288 and NGC 362 are less certain.

All the models are consistent in their relative age estimates: NGC 362 is  $2.6 \pm 0.5$  Gyr younger than NGC 288 and  $2.8 \pm 0.5$  Gyr younger than NGC 6218. Using the results from [Paper I](#), we find that NGC 362 is 1.15 Gyr younger than NGC 5904 with a similar metallicity. Taking into account the different HB morphology of these four GCs, our findings confirm the long-standing assumption that age is their second parameter.

Based on *Gaia* EDR3, we provide the lists of reliable members of the clusters and systemic proper motions with their systematic uncertainties in  $\text{mas yr}^{-1}$ :

$$\mu_\alpha \cos(\delta) = 4.147 \pm 0.024, \mu_\delta = -5.704 \pm 0.025$$

$$\mu_\alpha \cos(\delta) = 6.696 \pm 0.024, \mu_\delta = -2.543 \pm 0.024$$

$$\mu_\alpha \cos(\delta) = -0.204 \pm 0.024, \mu_\delta = -6.809 \pm 0.024$$

for NGC 288, NGC 362, and NGC 6218, respectively.

## ACKNOWLEDGEMENTS

We acknowledge financial support from the Russian Science Foundation (grant no. 20–72–10052).

We thank the anonymous reviewers for useful comments. We thank Charles Bonatto for discussion of differential reddening, Santi Casisi for providing the valuable BaSTI isochrones and his useful comments, Aaron Dotter for his comments on DSEP, Frank Grundahl for providing the Strömgren photometric data with their discussion, Christopher Onken and Sergey Antonov for their help to access the SkyMapper Southern Sky Survey DR3, Antonio Sollima for providing useful photometric results, Eugene Vasiliev for his useful comments. We thank Michal Rozyczka for providing the data for NGC 6218, which were gathered within the CASE project conducted at the Nicolaus Copernicus Astronomical Center of the Polish Academy of Sciences.

This research makes use of Filtergraph ([Burger et al. 2013](#)), an online data visualization tool developed at Vanderbilt University through the Vanderbilt Initiative in Data-intensive Astrophysics (VIDA) and the Frist Center for Autism and Innovation (FCAI, <https://filtergraph.com>). The resources of the Centre de Données astronomiques de Strasbourg, Strasbourg, France (<http://cds.u-strasbg.fr>), including the SIMBAD database, the VizieR catalogue access tool and the X-Match service, were widely used in this study. This work has made use of BaSTI and DSEP web tools. This work has made use of data from the European Space Agency (ESA) mission *Gaia* (<https://www.cosmos.esa.int/gaia>), processed by the *Gaia* Data Processing and Analysis Consortium (DPAC, <https://www.cosmos.esa.int/web/gaia/dpac/consortium>). The *Gaia* archive website is <https://archives.esac.esa.int/gaia>. This study is based on observations made with the NASA/ESA *Hubble Space Telescope*. This publication makes use of data products from the *Wide-field Infrared Survey Explorer*, which is a joint project of the University of California, Los Angeles, and the Jet Propulsion Laboratory/California Institute of Technology. This publication makes use of data products from the Pan-STARRS Surveys (PS1). This study makes use of data products from the SkyMapper Southern Sky Survey. SkyMapper is owned and operated by The Australian National University’s Research School of Astronomy and Astrophysics. The SkyMapper survey data were processed and provided by the SkyMapper Team at ANU. The SkyMapper node of the All-Sky Virtual Observatory (ASVO) is hosted at the National Computational Infrastructure (NCI).

## DATA AVAILABILITY

The data underlying this article will be shared on reasonable request to the corresponding author.

## REFERENCES

- Abbott T. M. C. et al., 2018, *ApJS*, 239, 18
- Anderson J. et al., 2008, *AJ*, 135, 2055
- Baumgardt H., Vasiliev E., 2021, *MNRAS*, 505, 5957
- Bellazzini M., Pecci F. F., Ferraro F. R., Galletti S., Catelan M., Landsman W. B., 2001, *AJ*, 122, 2569 (BPF01)
- Bernard E. J. et al., 2014, *MNRAS*, 442, 2999
- Bica E., Pavani D. B., Bonatto C. J., Lima E. F., 2019, *AJ*, 157, 12
- Bolte M., 1989, *AJ*, 97, 1688
- Bolte M., 1992, *ApJS*, 82, 145
- Bonatto C., Campos F., Kepler S. O., 2013, *MNRAS*, 435, 263
- Burger D., Stassun K. G., Pepper J., Siverd R. J., Paegert M., De Lee N. M., Robinson W. H., 2013, *Astron. Comput.*, 2, 40

- Cardelli J. A., Clayton G. C., Mathis J. S., 1989, *ApJ*, 345, 245 (CCM89)
- Carretta E., Bragaglia A., Gratton R., D’Orazi V., Lucatello S., 2009, *A&A*, 508, 695
- Carretta E., Bragaglia A., Gratton R. G., Recio-Blanco A., Lucatello S., D’Orazi V., Cassisi S., 2010, *A&A*, 516, A55
- Chambers K. C. et al., 2016, *arXiv:1612.05560*
- Cohen R. E., Hempel M., Mauro F., Geisler D., Alonso-Garcia J., Kineuchi K., 2015, *AJ*, 150, 176
- Davidge T. J., Harris W. E., 1997, *ApJ*, 475, 584
- de Boer T. J. L., Gieles M., Balbinot E., Hénault-Brunet V., Sollima A., Watkins L. L., Claydon I., 2019, *MNRAS*, 485, 4906
- Dotter A., Chaboyer B., Jevremović D., Baron E., Ferguson J. W., Sarajedini A., Anderson J., 2007, *AJ*, 134, 376
- Dotter A., Chaboyer B., Jevremović D., Kostov V., Baron E., Ferguson J. W., 2008, *ApJS*, 178, 89
- Fitzpatrick E. L., 1999, *PASP*, 111, 63
- Gaia collaboration, 2018, *A&A*, 616, A4
- Gaia collaboration et al., 2021a, *A&A*, 649, A2
- Gaia collaboration et al., 2021b, *A&A*, 649, A3
- Gaia collaboration et al., 2021c, *A&A*, 649, A4
- Goldsbury R., Richer H. B., Anderson J., Dotter A., Sarajedini A., Woodley K., 2010, *AJ*, 140, 1830
- Gontcharov G. A., Mosenkov A. V., 2017a, *MNRAS*, 470, L97
- Gontcharov G. A., Mosenkov A. V., 2017b, *MNRAS*, 472, 3805
- Gontcharov G. A., Mosenkov A. V., 2018, *MNRAS*, 475, 1121
- Gontcharov G. A., Mosenkov A. V., Khovritchev M. Yu., 2019, *MNRAS*, 483, 4949 (Paper I)
- Gontcharov G. A., Mosenkov A. V., Khovritchev M. Yu., 2020, *MNRAS*, 497, 3674 (Paper II)
- Gontcharov G. A., Mosenkov A. V., 2021, *MNRAS*, 500, 2590
- Gordon K. D. et al., 2011, *AJ*, 142, 102
- Grundahl F., Catelan M., Landsman W. B., Stetson P. B., Andersen M. I., 1999, *ApJ*, 524, 242 (GCL99)
- Hargis J. R., Sandquist E. L., Bolte M., 2004, *ApJ*, 608, 243 (HSB04)
- Harris W. E., 1996, *AJ*, 112, 1487
- Heber U., 2016, *PASP*, 128, 082001
- Hidalgo S. L. et al., 2018, *ApJ*, 856, 125
- Horta D. et al., 2020, *MNRAS*, 493, 3363
- Kaluzny J., Thompson I. B., Narloch W., Pych W., Rozyczka M., 2015, *Acta Astron.*, 65, 267
- Lardo C., Salaris M., Bastian N., Mucciarelli A., Dalessandro E., Cabrera-Ziri I., 2018, *A&A*, 616, A168
- Lee Y.-W., Demarque P., Zinn R., 1994, *ApJ*, 423, 248
- Libralato et al., 2018, *ApJ*, 861, 99
- Marín-Franch A. et al., 2009, *ApJ*, 694, 1498
- Marsakov V. A., Koval’ V. V., Gozha M. L., 2019, *Astron. Reports*, 63, 274
- Meisner A. M., Finkbeiner D. P., 2015, *ApJ*, 798, 88
- Milone A. P. et al., 2017, *MNRAS*, 464, 3636
- Milone A. P. et al., 2018, *MNRAS*, 481, 5098
- Monelli M. et al., 2013, *MNRAS*, 431, 2126
- Nardiello D. et al., 2018, *MNRAS*, 481, 3382
- O’Malley E. M., Gilligan C., Chaboyer B., 2017, *ApJ*, 838, 162
- Ochsenbein F., Bauer P., Marcout J., 2000, *A&AS*, 143, 221
- Onken C. A. et al., 2019, *Publ. Astron. Soc. Australia*, 36, 33
- Pietrinferni A. et al., 2021, *ApJ*, 908, 102
- Piotto G. et al., 2002, *A&A*, 391, 945
- Piotto G. et al., 2013, *ApJ*, 775, 15
- Reimers D., 1975, *Mem. Soc. R. Sci. Liege*, 8, 369
- Rosenberg A., Piotto G., Saviane I., Aparicio A., 2000, *A&AS*, 144, 5 (RPS00)
- Salaris M., Chieffi A., Straniero O., 1993, *ApJ*, 414, 580
- Savino A., Massari D., Bragaglia A., Dalessandro E., Tolstoy E., 2018, *MNRAS*, 474, 4438
- Schlafly E. F., Finkbeiner D. P., 2011, *ApJ*, 737, 103
- Schlafly E. F. et al., 2016, *ApJ*, 821, 78
- Schlafly E. F., Meisner A. M., Green G. M., 2019, *ApJS*, 240, 30
- Schlegel D. J., Finkbeiner D. P., Davis M., 1998, *ApJ*, 500, 525
- Simioni M. et al., 2018, *MNRAS*, 476, 271
- Skrutskie M. F. et al., 2006, *AJ*, 131, 1163
- Sollima A. et al., 2016, *MNRAS*, 462, 1937 (SFL16)
- Stetson P. B., Pancino E., Zocchi A., Sanna N., Monelli M., 2019, *MNRAS*, 485, 3042 (SPZ19)
- VandenBerg D. A., Brogaard K., Leaman R., Casagrande L., 2013, *ApJ*, 775, 134
- Vasiliev E., Baumgardt H., 2021, *MNRAS*, 505, 5978 (VB21)
- Vitral E., 2021, 504, 1355
- Wagner-Kaiser R., Stenning D. C., Sarajedini A., von Hippel T., van Dyk D. A., Robinson E., Stein N., Jefferys W. H., 2016, *MNRAS*, 463, 3768
- Wagner-Kaiser R. et al., 2017, *MNRAS*, 468, 1038
- Wang S., Chen X., 2019, *ApJ*, 877, 116
- Wright E. L. et al., 2010, *AJ*, 140, 1868
- Zaritsky D., Harris J., Thompson I. B., Grebel E. K., Massey P., 2002, *AJ*, 123, 855
- Zloczewski K., Kaluzny J., Rozyczka M., Krzeminski W., Mazur B., 2012, *Acta Astron.*, 62, 357 (ZKR12)

This paper has been typeset from a  $\text{\LaTeX}$  file prepared by the author.